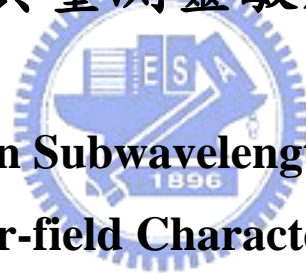


國立交通大學

光電工程研究所

博士論文

利用遠場特徵回溯次波長尺度變化
及提升其量測靈敏度之探討



**Investigations on Subwavelength-scale Variation
by Far-field Characteristics:**

Deconvolution and Detection Sensitivity Enhancement

研究生：朱淑君

指導教授：陳志隆教授

中華民國 九十五年 五月

利用遠場特徵回溯次波長尺度變化
及提升其量測靈敏度之探討

Investigations on Subwavelength-scale Variation
by Far-field Characteristics:
Deconvolution and Detection Sensitivity Enhancement

研究生：朱淑君
指導教授：陳志隆

Student : Shu-Chun Chu
Advisor : Jyh-Long Chern

國立交通大學
光電工程研究所
博士論文



Submitted to Department of Photonics, Institute of Electro-Optical Engineering
College of Electrical and Computer Engineering
National Chiao Tung University
in Partial Fulfillment of the Requirements
for the Degree of Doctor of Philosophy
in

Electro-Optical Engineering

2006

Hsinchu, Taiwan, Republic of China

中華民國 九十五年 五月

國立交通大學

博碩士論文全文電子檔著作權授權書

(提供授權人裝訂於紙本論文書名頁之次頁用)

本授權書所授權之學位論文，為本人於國立交通大學光電工程系所
_____組，94學年度第2學期取得博士學位之論文。

論文題目：利用遠場特徵回溯次波長尺度變化及提升其量測靈敏度
之探討

指導教授：陳志隆

■ 同意

本人茲將本著作，以非專屬、無償授權國立交通大學與台灣聯合大學系統圖書館：基於推動讀者間「資源共享、互惠合作」之理念，與回饋社會與學術研究之目的，國立交通大學及台灣聯合大學系統圖書館得不限地域、時間與次數，以紙本、光碟或數位化等各種方法收錄、重製與利用；於著作權法合理使用範圍內，讀者得進行線上檢索、閱覽、下載或列印。

論文全文上載網路公開之範圍及時間：

本校及台灣聯合大學系統區域網路	■ 中華民國 96 年 6 月 2 日公開
校外網際網路	■ 中華民國 96 年 6 月 2 日公開

■ 全文電子檔送交國家圖書館

授權人：朱淑君

親筆簽名：

朱淑君

中華民國

95 年 6 月 2 日

國立交通大學

博碩士紙本論文著作權授權書

(提供授權人裝訂於全文電子檔授權書之次頁用)

本授權書所授權之學位論文，為本人於國立交通大學光電工程系所
_____組，94學年度第2學期取得博士學位之論文。

論文題目：利用遠場特徵回溯次波長尺度變化及提升其量測靈敏度
之探討

指導教授：陳志隆

■ 同意

本人茲將本著作，以非專屬、無償授權國立交通大學，基於推動讀者間「資源共享、互惠合作」之理念，與回饋社會與學術研究之目的，國立交通大學圖書館得以紙本收錄、重製與利用；於著作權法合理使用範圍內，讀者得進行閱覽或列印。

本論文為本人向經濟部智慧局申請專利(未申請者本條款請不予理會)的附件之一，申請文號為：_____，請將論文延至____年____月____日再公開。

授權人：朱淑君

親筆簽名：

朱淑君

中華民國

95年6月2日

國家圖書館 博碩士論文電子檔案上網授權書

(提供授權人裝訂於紙本論文本校授權書之後)

ID:GT009224805

本授權書所授權之論文為授權人在國立交通大學光電工程系所 94 學年度第 2 學期取得博士學位之論文。

論文題目：利用遠場特徵回溯次波長尺度變化及提升其量測靈敏度之探討

指導教授：陳志隆

茲同意將授權人擁有著作權之上列論文全文（含摘要），非專屬、無償授權國家圖書館，不限地域、時間與次數，以微縮、光碟或其他各種數位化方式將上列論文重製，並得將數位化之上列論文及論文電子檔以上載網路方式，提供讀者基於個人非營利性質之線上檢索、閱覽、下載或列印。

※ 讀者基於非營利性質之線上檢索、閱覽、下載或列印上列論文，應依著作權法相關規定辦理。

授權人：朱淑君

親筆簽名：朱淑君

民國 95 年 6 月 2 日

國立交通大學

論文口試委員會審定書

本校光電工程研究所博士班 朱淑君 君

所提論文 利用遠場特徵回溯次波長尺度變化及提升其量測靈敏度之探討

合於博士資格標準、業經本委員會評審認可。

口試委員：黃中焄

黃中焄 教授

許根玉

許根玉 教授

蘇德欽

蘇德欽 教授

賴映杰

賴映杰 教授

朱國瑞

朱國瑞 教授

施宙聰

施宙聰 教授

指導教授：陳志峰

所長：賴映杰 教授

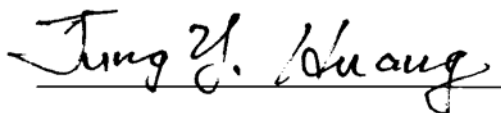
系主任：馮厚靈 教授

中華民國 95 年 5 月 30 日


Institute of Electro-Optical Engineering
National Chiao Tung University
Hsinchu, Taiwan, R.O.C.

Date : May 30, 2006

We have carefully read the dissertation entitled Investigations on
Subwavelength-scale Variation by Far-field Characteristics: Deconvolution and
Detection Sensitivity Enhancement submitted by Shu-Chun Chu in partial
fulfillment of the requirements of the degree of DOCTOR OF PHILOSOPHY and
recommend its acceptance.



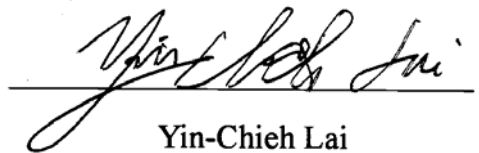
Jung Y. Hohn Huang



Ken Y. Hsu



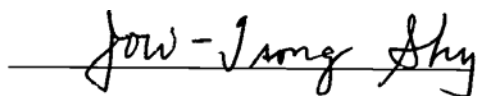
Der-Chin Su



Yin-Chieh Lai



Kwo-Ray Chu



Jow-Tsong Shy

Thesis Advisor : Jyh-long Chern

Director of Institute of Electro-Optical Engineering : Yin-Chieh Lai

Chairman of Department of Photonics : Pan Ci-lin

利用遠場特徵回溯次波長尺度變化及 提升其量測靈敏度之探討

博士研究生：朱淑君

指導教授：陳志隆教授

國立交通大學

光電工程研究所

摘 要

由於奈米科技、生醫檢測諸多領域的蓬勃發展，次波長尺度的量測也愈見其重要性。有鑑於此，許多高空間解析度的探針掃描或近場的量測方法陸續被開發出來。以往，在遠場量測次波長尺度的資訊被視作困難或不可行。然而在 Selci 等前人的工作中，實驗發現在遠場仍可觀測到物體在次波長尺度變化下相應的光學特徵變化，並滿足純量光學理論的預測。其結果隱含著在遠場利用光學方式去量測物體的次波長尺度動態變化的潛力。基於遠場的光學量測方式具有易於觀測，且不易傷害待測物的優點，因此本論文探討了利用遠場的光學特徵去回溯出待測物的次波長尺度動態變化的可行性及其測量方式。

本論文對利用遠場的光學特徵去回溯出待測物的次波長尺度變化作了下列的初步探討：（一）提出利用遠場輻照度的變化，去回推物體作一維次波長尺度變化的算則，其精準度可到一個奈米的等級。（二）提出一外加孔徑干涉儀的架構，可對任意待測孔徑寬度優化其遠場量測到的輻照度變化量值，而可提高其一維次波長尺度動態變化的測量靈敏度。（三）提出利用未知訊號分離的手法，利用多光偵測器及外加孔徑干涉儀的架構，去回推孔徑兩個維度的次波長尺度動態變化，其精準度可到 1%。（四）利用量測遠場輻照度回推孔徑一維次波長尺度動態變化的手法，提出了一個可量測待測物的邊緣平整度誤差低於 3% 的量測架構。

由本論文的探討，展現了利用遠場光學特徵去回溯物體次波長尺度動態變化的應用潛力。對於利用遠場光學特徵去量測真實的待測結構及其工程上的量測應用將是未來值得被探討的重點課題。

Investigations on Subwavelength-scale Variation by Far-field Characteristics: Deconvolution and Detection Sensitivity Enhancement

Doctoral Student: Shu-Chun Chu **Advisor:** Dr. Jyh-Long Chern

**Institute of Electro-Optical Engineering
National Chiao Tung University**

Abstract

The advance of the nanotechnology and bio-measurement highlight the importance of the measurement within the scale of subwavelength. Thus, several scanning probe microscope methods or near-field measurements have been developed to achieve high spatial resolution. In the past, the extraction of subwavelength information from far-field measurement was generally believed to be very difficult or perhaps impossible. However, the recently experimental result of Selci and Righini demonstrated that to detect subwavelength information in the far-field is possible and fully consistent with the prediction of the standard scalar diffraction theory. The result highlighted the possibility of measuring optical signals in the far field with sufficient sensitivity to show variations of diffraction structure in subwavelength scale. We believe that the far-field optical measurement was provided as a potential approach to have high-precision measure of subwavelength-scale dynamical variation of structure, accompanying the advantages of less damage on sample and facility in realization. Thus in this thesis, we investigate the possibility and approaches to retrieve subwavelength-scale dynamical variation from the measurement of far-field optical characteristics.

The thesis provides some preliminary discussions on retrieving subwavelength-scale variation by far-field characteristics. (1) An approach to retrieve 1-D subwavelength feature variation from far-field irradiance measurement was proposed and was numerically verified which could have precision better than 1 nm. (2) A tunable asymmetrical embedded-aperture interferometer configuration was proposed, which could enhance detection sensitivity of 1-D subwavelength variation measurement at arbitrary aperture width. (3) A multi-detector, embedded-aperture interferometer configuration accompanies blind signal separation method was proposed could recover coupled 2-D subwavelength variation information of a rectangular

aperture with far-field irradiance measurement with error ratio below 1%. (4) By using the approach to retrieve 1-D subwavelength variation from far-field irradiance measurement, a constructed-aperture measurement system behaving as an optical ruler was proposed, which could measure the marginal roughness of the test sample with error ratio below 3%.

From the discussions in this thesis, we demonstrated that the far-field optical measurement was provided as a potential approach to have high-precision measure of subwavelength-scale dynamical variation of structure. To explore to test sample with realistic structures and to do more engineering applications are important issues which should be investigated in the future.



誌 謝

一轉眼，加入陳志隆教授的研究群已經三年了。在這些年的研究當中，要感謝的人真的很多，僅以此文表達我的誠摯謝意。

我衷心的感謝陳志隆教授在研究上、表達能力上、甚至生活細節上的悉心指導，讓我在十分優良的研究環境下成長、學習。在這三年的研究生活中，要感謝鄭伊凱學長，一同奮鬥的介仁、兆璽，彼此間的相互討論與扶持，是這幾年研究生活裡很大的助益。另外，對於許多已經畢業以及目前在這個實驗室繼續奮鬥的優秀碩士班學弟妹們，謝謝你們一同經營了這個溫馨且愉快的研究環境，讓我三年來的研究生活充滿了美好的回憶。而這些日子裡，真的很感謝我的好友，婕琳、玉棉，在我最低潮的時候有妳們陪我一起渡過，開心的時候有妳們跟我一起分享，讓我一路走來不覺孤單。

對於我最親愛的父母親，真的謝謝你們二十多年來對我的栽培，在未來的日子裡我必當竭盡所能來報答你們、孝順你們。謝謝我的家人在這一路上給我的支持與鼓勵，讓我有勇氣邁入人生的另一個階段。我愛你們。謝謝所有關心我、愛護我的人對我所付出的一切，讓我在此致上我最誠摯的感謝。



Table of Contents

Abstract (Chinese)	i
Abstract (English)	ii
Acknowledgement	iv
Table of Contents	v
Figure Caption	viii
Chapter 1 Introduction	1
1.1 Background and motivation.....	1
1.2 Objective of this thesis.....	3
1.3 Organization of this thesis.....	4
Chapter 2 Retrieving of 1-D subwavelength variation information	5
2.1 Introduction.....	5
2.2 Retrieving 1-D subwavelength signature from far-field irradiance measurement	5
2.2.1 Basic assumptions.....	6
2.2.2 Simulation verification with subwavelength variation.....	9
2.3 Retrieving 1-D subwavelength signature from far-field diffraction pattern measurement	12
2.3.1 Basic assumptions.....	13
2.3.2 Simulation verification with subwavelength variation.....	17
2.3.3 Discussion on contrast influence in pattern measurement.....	20
2.4 Summary	22
Chapter 3 Enhancement of detection sensitivity of 1-D subwavelength variation measurement	24
3.1 Introduction.....	24
3.2 Symmetrically-embedded-aperture interferometer.....	25

3.2.1 Basic formalism and general features	25
3.2.2 Simulation verification and discussion	29
3.3 Tunable asymmetrically-embedded-aperture interferometer	32
3.3.1 Basic formalism and general features	32
3.3.2 Detection sensitivity optimization	38
3.3.3 Discussion	40
3.4 Summary	45
Chapter 4 Deconvolution of 2-D subwavelength variation information	46
4.1 Introduction	46
4.2 Retrieving 2-D subwavelength variation characteristics with two-detector strategy	47
4.2.1 Basic formalism and general features	47
4.2.2 Time-delayed correlation methods	49
4.2.3 Retrieving results and scaling issues	50
4.3 Three-detector embedded-aperture interferometer configuration	53
4.3.1 Basic formalism and general features	53
4.3.2 Simulation verification and Discussions	56
4.4 Summary	59
Chapter 5 1-D Marginal Roughness Measurement	61
5.1 Introduction	61
5.2 Constructed-aperture roughness measurement system	61
5.3 Thickness effect of test sample	65
5.4 Simulation verifications and discussions	68
5.5 Summary	72
Chapter 6 Conclusions and Future Works	73
6.1 Conclusions	73
6.1.1 Retriving of 1-D subwavelength variation information	74
6.1.2 Enhancement of detection sensitivity of 1-D subwavelength variation measurement	75

6.1.3 Deconvolution of 2-D subwavelength variation information	76
6.1.4 One-dimension Marginal Roughness Measurement	77
6.2 Future works	78
Reference	81
Appendix I: Review of scalar diffraction theorem	85
Appendix II : Blind source separation problem	95
Publication List	102



Figure Captions

Fig. 2-1. Schematic diagram of the variation diffraction structures6

Fig. 2-2. (a) Schematic diagram of the variation of function $Si(2kaX/z)$ (b) enlargement of part of the Fig. 2-2 (a).....8

Fig. 2-3. Deduced subwavelength variation, a^* , and the difference between the deduced value and the simulation-setting value, a^*-a , for a slit. (a), (b): periodic, (c), (d): quasi-periodic, and (e), (f): random fluctuation.. 10

Fig. 2-4. Subwavelength variation for a rectangular aperture. (a): deduced a^* , (b): the difference a^*-a , where the dotted curve refers to the periodic case, the solid-line curve refers to the quasi-periodic case and the bold solid-line curve refers to the random case. 11

Fig. 3-1 Schematic diagram of interferometer configuration26

Fig. 3-2 Derivative intensity versus the half aperture width. The maximum sensitive observation half aperture was optimized at (a) $50\ \mu m$, (b) $100\ \mu m$, and (c) $150\ \mu m$ 31

Fig. 3-3.Schematic diagram of interferometer configuration.. 33

Fig. 3-4. Derivative intensity versus the half aperture width. The maximum sensitive observation half aperture was optimized at (a) $50\ \mu m$, (b) $100\ \mu m$, and (c) $150\ \mu m$ 33

Fig. 3-5. (a) Schematic diagram of interferometer configuration. (b) The relative position of the detected-aperture. (c) The relative position of the embedded-aperture.....40

Fig. 3-6. Normalized derivative intensity versus the test aperture width. The reference aperture width: $150\ \mu m$, relative position: (a) $50\ \mu m$, (b) $150\ \mu m$, and (c) $250\ \mu m$. The relative position of the reference aperture: $250\ \mu m$, with width: (d) $50\ \mu m$, (e) $150\ \mu m$, and (f) $250\ \mu m$ 41

Fig. 3-7. Normalized derivative intensity versus the test aperture width. The maximum sensitive detected-aperture width was optimized at (a) $100\ \mu m$, (b)

300 μm , and (c) 500 μm	43
Fig. 4-1. Schematic diagrams of (a) a two-detector configuration, while (b) shows the relative positions of two detectors	47
Fig. 4-2. Schematic diagrams of the blind signal separation problems	49
Fig. 4-3. The results of two-detector configuration. (a) the setting and retrieving aperture width variations: Δa and $\Delta a'$, and (b) the setting and retrieving aperture width variations: Δb and $\Delta b'$	52
Fig. 4-4. Schematic diagrams of (a) an embedded-aperture three-detector interferometer while (b) shows the relative positions of the detectors. (c) Schematic diagram of the sizes of the two apertures.....	53
Fig. 4-5.(a): The inverse mean error of the retrieving embedded-aperture variation versus the time delay, τ . (b) the error and error percentage between setting and retrieving aperture width variations: Δa and $\Delta a'$, (c) the error and error percentage between setting and retrieving aperture width variations: Δb and $\Delta b'$	58
Fig. 5-1. Schematic diagrams of (a) constructed-aperture marginal roughness measurement system, (b) a front view of the constructed aperture of the system.	63
Fig. 5-2. Schematic diagram of a side view of the constructed-aperture marginal roughness measurement system.....	66
Fig. 5-3. The retrieving results of two different marginal roughness profiles: (a) sine variation. (b) quasi-periodic variation... ..	70
Fig. 6-1. The flow chart of my future works.....	80

Chapter 1

Introduction

1.1 Background and motivation

The progress in scientific research and industry, such as nanotechnology ^[1], nanobiology ^[2], material science ^[3], semi-conductor manufacturing ^[4], and several others prompt the developments in measurement technology at subwavelength scale.

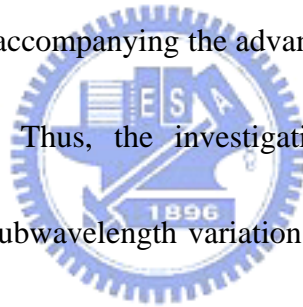
In the past, the extraction of subwavelength information from *far-field* optical measurement was generally believed to be very difficult or perhaps impossible. This is according to the reason that the wave information containing structure finest details is carried by evanescent wave, which decaying exponentially and was hard to be detected in the far-field ^[5,6,7]. Owing to that reason, several non-optical scanning probe microscope (SPM) skills and applications have been developed to achieve high spatial resolution, such as: Atomic Force Microscopy (AFM) ^[8,9], Scanning Tunneling Microscopy (STM) ^[10,11], or implementing the measure in the Near-field, such as Near-Field Scanning Optical Microscopy (NSOM) ^[12,13].

However, the recently experimental result of Selci and Righini highlighted that

to detect subwavelength information in the far-field is possible and fully consistent with the prediction of the standard scalar diffraction theory ^[14]. Scalar theory is accurate when the diffracting structures are much larger comparing with the wavelength of light ^[15], and could be used to predict the far-field optical characteristics. In the research of Selci and Righini, they answered an interesting question that *“while the diffraction feature size fulfills with the assumption of the scalar diffraction theory and was varying in subwavelength scale, does such smaller variation can influence the corresponding far-field characteristics and could be measured in a detectable way?”* Their experimental result demonstrated that, when the width of the diffraction feature size exceeds several wavelengths, subwavelength-scale size variations of an object even at nano-scale can affect the corresponding far-field diffraction pattern in a measurable way; its far-field characteristics of integrative intensity and derivative intensity are consistent with the prediction of the scalar diffraction theory, even when the size variation is in the order of 1/100 wavelength. This result highlighted the possibility of measuring optical signals in the far field with sufficient sensitivity to show subwavelength-scale variations of diffraction structure.

To detect the far-field characteristics that correspond to subwavelength-scale

variation has been proved to be possible; the retrieving of dynamic *signature* of subwavelength variation yields some more interesting information than the static features, particularly in determining physical origins and in identifying the generation mechanism. The recently advance of bio-technology emphasized the requests and needs of subwavelength-scale measurement ^[16,17,18]. Some bio-samples, such as cells, are usually in the scale exceeding several wavelengths, and are varying in wavelength or subwavelength scale dynamically. We believe that the far-field optical measurement can be considered as a potential approach to have high-precision dynamical measurement, and accompanying the advantages of less damage on sample and facility in realization. Thus, the investigation and development of new approaches in retrieving the subwavelength variation signal by using optical method in the far-field is important and deserved to explore.



1.2 Objective of this thesis

A prior research had demonstrated to detect subwavelength signal in the far-field is possible while the diffraction structure size fulfills with the assumptions of scalar diffraction theory. It highlighted the possibility of measuring optical signals in far-field with sufficient sensitivity to show variations that are orders of magnitude below the wavelength of light. A further question we want to know is that if it is

possible to retrieve subwavelength-scale variation only by measuring far-field characteristics. Thus, in this thesis, we want to investigate the possibility and the schemes to retrieve subwavelength dynamic signatures of diffraction structure with the measurement of optical characteristics in the far-field.

1.3 Organization of this thesis

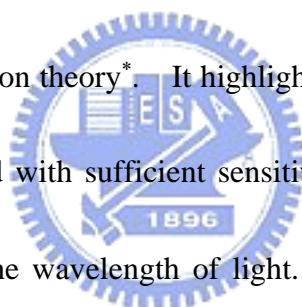
The thesis is organized as following: The possibility verification and an approach to retrieve 1-D subwavelength feature variation from far-field optical measurement will be shown in **Chapter 2**. In **Chapter 3**, a tunable asymmetrically embedded-aperture interferometer configuration was proposed to enhance detection sensitivity of 1-D subwavelength variation measurement. A three-detector, embedded-aperture interferometer configuration accompany blind signal separation method was proposed to recover 2-D subwavelength variation information of a rectangular aperture with far-field irradiance measurement was shown in **Chapter 4**. In **Chapter 5**, a constructed-aperture measurement system behaving as an optical ruler to measure the marginal roughness of the test sample with error ratio below 3% was proposed. Finally, a summary of this dissertation, and the future works are presented in **Chapter 6**.

Chapter 2

Retrieving of 1-D subwavelength variation information

2.1 Introduction

Recently, to detect subwavelength signal in the far-field is experimentally demonstrated to be possible while the diffraction structure size are fulfill with the assumptions of scalar diffraction theory*. It highlighted the possibility of measuring optical signals in the far field with sufficient sensitivity to show variations that are orders of magnitude below the wavelength of light. Could we retrieve it only by measuring far-field characteristics? With the academic aim of clarifying this point, we investigated to retrieve subwavelength dynamic variations of the most simple diffraction structures, slit and rectangular aperture. In this chapter, it will be shown that the 1-D subwavelength variation information is retrievable from far-field characteristics measurement.



2.2 Retrieving 1-D subwavelength signature from far-field irradiance

* A brief review of scalar diffraction theorem could be found in Appendix II.

measurement

In section 2.2, a method was proposed to retrieve subwavelength variation of the diffraction structure by measuring far-field irradiance variation. The 1-D dynamic signature of the subwavelength variation of the simplest geometric structures, a slit and rectangular aperture, will be shown to be determinable from far-field irradiance with a precision of better than 1 nm ^[19].

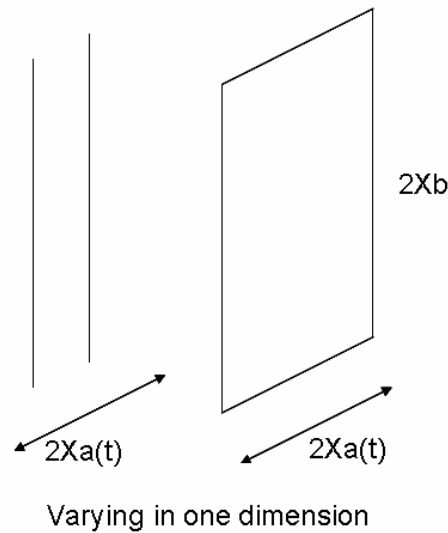


Fig. 2-1. Schematic diagram of the variation diffraction structures

2.2.1 Basic assumptions

A physical quantity, *derivative intensity*, of these two simple diffraction situations was deduced to retrieve the subwavelength variation of these two diffraction structures. Considering the most simple situation that a monochromatic

plane wave of amplitude A and a wavelength λ is assumed to orthogonally illuminate on a rectangular aperture, with dimensions $2a$ and $2b$. The observation plane was positioned at a distance z away from the aperture. The diffracted intensity was collected over a rectangular detector with dimensions $2X$ and $2Y$ centered at the origin of the observation plane. The far-field intensity distribution on the detector is given by the expression^[20]

$$I(x, y) = \left(\frac{4A}{\lambda z}\right)^2 \frac{\sin^2(kax/\lambda z)}{(kx/z)^2} \frac{\sin^2(kby/\lambda z)}{(ky/z)^2}. \quad (2-1)$$

The overall power P_z , flowing through the collection region is given by

$$P_z = \int_{-a}^a \int_{-b}^b I(x, y) dx dy.$$

And the physical quantity that **derivative intensity** was defined as the derivative of P_z with respect to aperture width a , $\frac{dP_z}{da}$. The derivative

intensities of these two situations could be derived as:

$$\left\{ \begin{array}{l} \frac{dP_z}{da} = \frac{8A^2b}{\pi} Si\left(\frac{2kaX}{z}\right) \dots\dots\dots \text{slit} \\ \frac{dP_z}{da} = \frac{8A^2z\lambda}{\pi^3} f_p\left(Y, \frac{kb}{z}\right) Si\left(\frac{2kaX}{z}\right) \dots\dots\dots \text{rectangular aperture} \end{array} \right., \quad (2-2)$$

where Si is the sine-integral function, and the function f_p was defined and could be evaluated by Leibniz Integral Rule^[21] as $f_p(X, a) = \int_0^X \frac{\sin^2(ax)}{x^2} dx = aSi(2aX) - \frac{\sin^2(aX)}{X}$.

The derivative intensities of the two diffraction structure are both proportional to the function $Si\left(\frac{2kaX}{z}\right)$, which was shown in the Fig. 2-2 (In this demonstrated

figure, X is $100\ \mu\text{m}$, z is $100\ \text{mm}$, and light source wavelength of $632.8\ \text{nm}$ was used.). It could be found that the fluctuations of derivative intensities were very small while the width of the diffraction structure is varying in the subwavelength scale. We make the assumption that *while the width of the diffraction structure is varying in subwavelength scale, the variation of derivative intensity is small enough to be estimated as a constant value.*

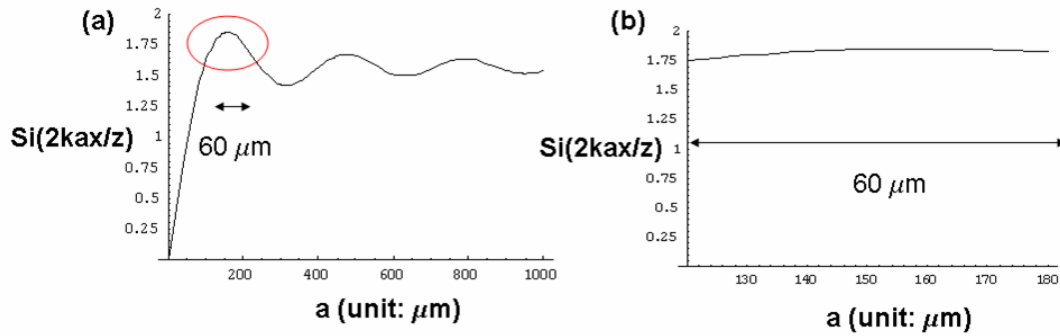


Fig. 2-2. (a) Schematic diagram of the variation of function $Si(2kaX/z)$ (b) enlargement of part of the Fig. 2-2 (a)

Thus, the equation will approximately hold

$$\left(\frac{da}{dt}\right)_t \cong \left(\frac{dP_z}{dt}\right)_t / \left(\frac{dP_z}{da}\right)_{a_0} = C_0 \left(\frac{dP_z}{dt}\right)_t. \quad (2-3)$$

The derivative intensity $\left(\frac{dP_z}{da}\right)_{a_0}$ can be evaluated analytically and is a constant,

whereas the temporal variation of power $\left(\frac{dP_z}{dt}\right)_t$ on the detector can be measured.

Therefore, Eq. (2-3) could be used to deduce the rate of variation of the width of the

slit $\left(\frac{da}{dt}\right)_t$, so does the aperture width variation: $\Delta a \approx \left(\frac{da}{dt}\right)_t * \Delta t$.

2.2.2 Simulation verification with subwavelength variation

Three different typical cases - periodic, quasi-periodic, and random variations - were used to investigate the feasibility of the proposed retrieving method. In the simulation, the amplitude of the vibration was taken to be 10 nm at a frequency of 100 Hz . The sampling rate of detector was 1.0 KHz , which is higher than the frequency of the vibration of the slit. The half-width of the slit a was $50\text{ }\mu\text{m}$. The half width of the detector, X and Y were both $100\text{ }\mu\text{m}$; the detector was placed behind the lens with a focal length of 30 mm . A light source wavelength of 632.8 nm was used.

The sine function was used to represent the periodic subwavelength variation: the slit variation then would be, $a(t) = a_0 + \alpha \times \sin(2\pi ft)$, where α was the amplitude of the vibration of the slit. The quasi-periodic subwavelength variation of the slit is given by $a(t) = a_0 + \alpha \times \sin(2\pi ft) + \alpha \times \sin(2\pi\sqrt{2}ft)$. The random fluctuation is specified by $a(t + \Delta t) = a(t) + \alpha \times \eta$, where η is a randomly selected value ranging from -1 to 1. Numerically, we know the exact width of the aperture

along the x direction from time to time, which is referred to as the simulation-setting value of the width of the slit. Figure 2-3 shows the relation between the deduced value and the simulation-setting value by the method we used. The curves on the left plot the deduced variation of the width of the slit, a^* , and the curves on the right plot the difference between the deduced value and the simulation-setting value, $a^*(t) - a(t)$. The difference between the deduced and the simulation-setting values is about $10^{-6} nm$. It means that the method of deduction is with very high precision, and the inaccuracy is only about 10^{-7} of the vibration amplitude of $10 nm$.

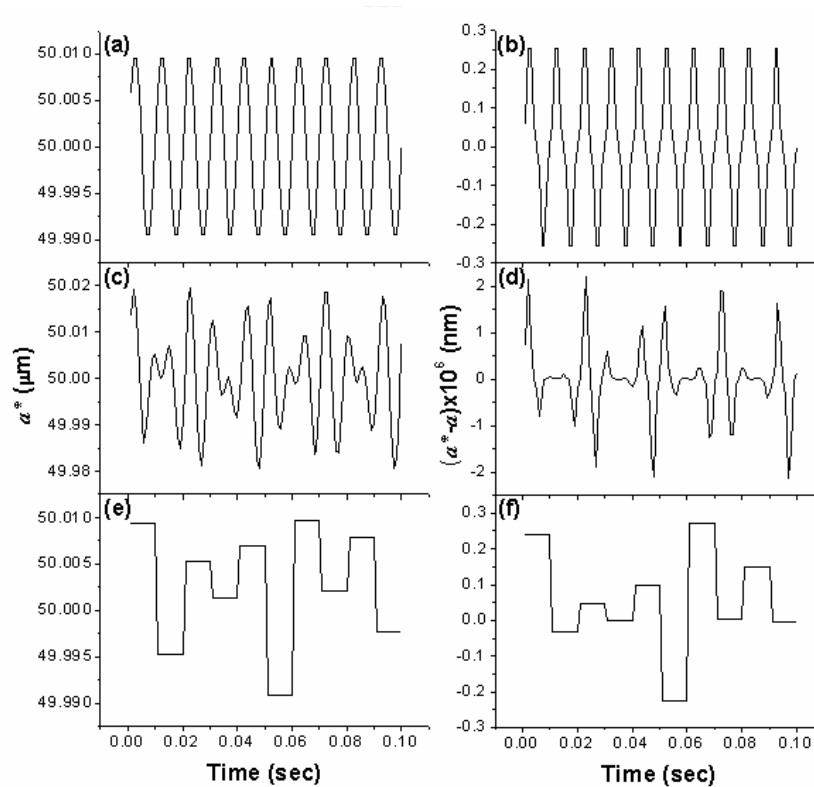


Fig. 2-3. Deduced subwavelength variation, a^* , and the difference between the deduced value and the simulation-setting value, $a^* - a$, for a slit. (a), (b): periodic, (c), (d): quasi-periodic, and (e), (f): random fluctuation.

In the simulation of the rectangular diffraction aperture, all simulation settings were same as that of slit case, except the aperture widths a and b were both set to $50\ \mu\text{m}$. As shown in Fig. 2-4, the difference between the deduced value and the simulation-setting value remained far below $1\ \text{nm}$ (specifically, about $10^{-5}\ \text{nm}$). In other words, in the case of a general rectangular aperture, subwavelength variation can be retrieved precisely from the far-field irradiance. Extensive simulations revealed that in the general case of a light diffracting rectangular aperture, even when the vibration amplitude is $1\ \mu\text{m}$, the inaccuracy remains below $1\ \text{nm}$.

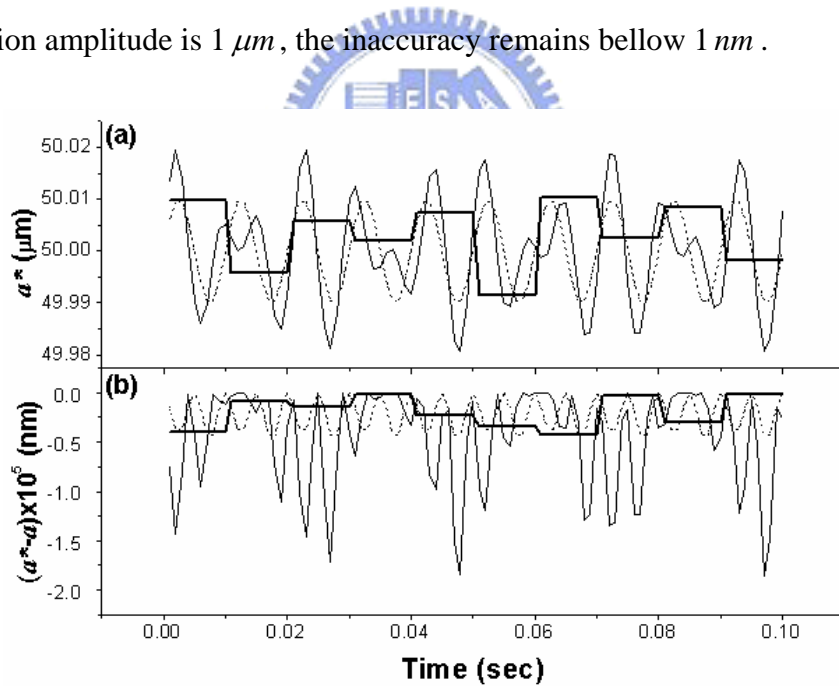


Fig. 2-4. Subwavelength variation for a rectangular aperture. (a): deduced a^* , (b): the difference $a^* - a$, where the dotted curve refers to the periodic case, the solid-line curve refers to the quasi-periodic case and the bold solid-line curve refers to the random case.

2.3 Retrieving 1-D subwavelength signature from far-field diffraction pattern measurement

In the section 2.2, the 1-D dynamic subwavelength variation signature is shown to be determinable a precision of better than 1 nm from far-field irradiance measurement by using the deduced quantity, derivative intensity. We may ask if there is any other quantity that could be used to retrieve the subwavelength variation of diffraction structure, besides the quantity of derivative intensity. Truly, derivative intensity is not the only far-field optical quantity of characterization. In addition, we have an alternative characterization with far-field diffraction pattern. The subwavelength variation of diffractive structure causes the variation in the far-field diffraction pattern. Hence, one can retrieve the information contained in the far-field diffraction pattern and use it to trace the scale of subwavelength variation. In the section 2.3, it will be shown that the associated shifting of the *dark line* of diffraction pattern, caused by subwavelength variation, had good linear correlation to that and will be magnified about hundred times. Hence, an alternative method of detecting subwavelength variation from far-field measurement, based on pattern measurement could be achieved.

2.3.1 Basic formalism

The basic formalism of associated shifting of the *dark line* of diffraction pattern to the corresponding 1-D subwavelength variation in two situations: (1) Direct observing the diffraction pattern, and (2) Observing interference pattern with an embedded aperture, will be addressed in this section.

(a) Directly observing the diffraction pattern

Consider the optical wave diffracted by a single aperture with the dimensions $2a$ and $2b$. The intensity distribution on the detector that positioned at a distance z away from the aperture is

$$I(x, y) = \left(\frac{4A}{\lambda z} \right)^2 \frac{\sin^2(kax/z)}{(kx/z)^2} \frac{\sin^2(kby/z)}{(ky/z)^2}. \quad (2-4)$$

The analytical result of the dark line locations on the detector along the x direction is

$$x_d(a) = \frac{m\lambda z}{2a}, \quad (m = 1, 2, 3, \dots) \quad (2-5)$$

, where m is the order of dark line pattern. Expanding the width at a certain specified aperture width, e.g., $a = a_0$, we have

$$x_d(a) = \frac{m\lambda z}{2} \left[\left(\frac{1}{a_0} - \frac{1}{a_0^2}(a - a_0) + \frac{1}{a_0^3}(a - a_0)^2 + O(a - a_0)^3 \right) \right], \quad (2-6)$$

where the symbol O denotes the truncated terms after the second order $(a - a_0)^2$.

Apparently, when the aperture has a subwavelength variation and the diffraction aperture is much larger compared to the wavelength of light, then under the first order approximation, the relation between the pattern shift on the screen, Δx_d , and the subwavelength variation Δa is

$$\Delta x_d \cong -\frac{m\lambda z}{2a_0^2} \Delta a. \quad (2-7)$$

The inaccuracy ratio of the approximation is $\sim |a - a_0|/a_0$.

(b) Observing interference pattern with an embedded aperture

In this section, we consider the diffraction pattern variation under embedded-aperture interferometer configuration. As shown in Fig. 2-5, it is a common Mach-Zehnder interferometer but with an embedded aperture. To be specific, a monochromatic plane wave of amplitude A and wavelength λ was assumed to be orthogonally illuminated on a beam splitter B_1 . The beam was split into two after passing through the beam splitter. One beam was reflected by a mirror M_1 , and passed through a rectangular observation aperture S_1 , with dimensions $2a$ and $2b$. Another beam was reflected by mirror M_2 , and passed through another rectangular embedded aperture S_2 , whose dimensions were $2a'$ and $2b$. (For simplicity, we set the two apertures to be different in one direction only.) Then the two beams were passed through another beam splitter B_2 and recombined into one

beam. The diffracted intensity was collected over a rectangular detector. The detector was with dimensions $2X$ and $2Y$ centered at the beam width, and was positioned at a path distance z away from each aperture.

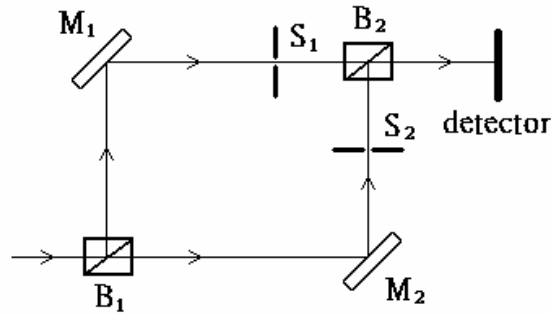


Fig. 2-5. Schematic diagram of embedded-aperture interferometer configuration

The interference intensity distribution of these two beams on the detector is

$$I(x, y) = |U_1 + U_2|^2 = \left(\frac{4A}{\lambda z} \right)^2 \frac{\sin^2(kby/z)}{(ky/z)^2} \left[\frac{\sin^2(kax/z)}{(kx/z)^2} + \frac{\sin^2(ka'x/z)}{(kx/z)^2} + 2 \frac{\sin(kax/z)\sin(ka'x/z)}{(kx/z)^2} \right]. \quad (2-8)$$

Assuming that there is subwavelength variation along the x direction for the observation aperture with dimensions $2a$ and $2b$, where $a = a_0 + \Delta a$ and the symbol Δa denotes the subwavelength variation of the half aperture-width. The other beam passes through another embedded rectangular aperture, with dimensions $2a'$ and $2b$, where $a' = a_0$. Explicitly, from Eq. (2-8), the interference intensity distribution of these two beams on the detector can be rewritten as:

$$I(x, y) = \frac{16A^2 \sin^2(kby/z)}{(\lambda z)^2 (ky/z)^2} \frac{1}{(kx/z)^2} \{ \sin(ka_0x/z) + \sin[k(a_0 + \Delta a)x/z] \}^2, \quad (2-9)$$

$$= C \{ \sin(ka_0x/z) + \sin[k(a_0 + \Delta a)x/z] \}^2$$

where the symbol C denotes the function which has no relationship to the widths along x-direction of the two apertures. Therefore, one can use Eq. (2-9) to solve the numerical result of the dark line locations of the interference pattern. The condition follows that

$$\frac{\partial I}{\partial x} = 0 \quad \text{and} \quad \frac{\partial^2 I}{\partial x^2} > 0. \quad (2-10)$$

Assuming that the variation scale, compared to the aperture width for the observing subwavelength variation was very small, we can deduce the linear relation between the subwavelength variation of the half aperture-width and the dark-line pattern shift as follow. The function $\sin[k(a_0 + \Delta a)x/z]$ was expanded to $\sin(ka_0x/z)\cos(k\Delta ax/z) + \cos(ka_0x/z)\sin(k\Delta ax/z)$. Considering the variation of the half aperture in the subwavelength scale, with substitutions $\cos(k\Delta ax/z) \approx 1$ and $\sin(k\Delta ax/z) \approx k\Delta ax/z$, the interference intensity can be rewritten as $I(x, y) = C \{ 2\sin(ka_0x/z) + (k\Delta ax/z) \times \cos(ka_0x/z) \}^2$. The relations between the dark-line position x_d axis and the subwavelength variation Δa is

$$\tan(ka_0x_d/z) = -k\Delta ax_d/2z. \quad (2-11)$$

The pattern shift $\Delta x_d = \frac{dx_d}{da} \Delta a$, where $\frac{dx_d}{da} = \frac{dx_d}{d(a_0 + \Delta a)} = \frac{dx_d}{d(\Delta a)}$. Derived from Eq. (2-11) with Δa , we have

$$\frac{dx_d}{da} = \frac{dx_d}{d(\Delta a)} = \frac{-kx_d/2z}{\frac{k\Delta a}{2z} + \frac{ka_0}{z} \sec^2\left(\frac{ka_0x_d}{z}\right)} \approx -\frac{x_d/2a_0}{\sec^2\left(\frac{ka_0x_d}{z}\right)}, \quad (2-12)$$

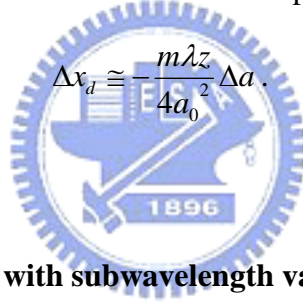
where the $\sec^2\left(\frac{ka_0x_d}{z}\right) = 1 + \tan^2\left(\frac{ka_0x_d}{z}\right)$. From Eq. (2-11), we obtain the relation

$\tan^2\left(\frac{ka_0x_d}{z}\right) = (-k\Delta ax_d/2z)^2$. Because the variation of the aperture was in the subwavelength scale, $\tan^2\left(\frac{ka_0x_d}{z}\right) \ll 1$ and $\sec^2\left(\frac{ka_0x_d}{z}\right)$ can be approximated to 1.

Considered with $a \approx a'$, the dark-line position x_d is very close to the value that was diffracted by the single aperture with half width a_0 , with a substitution x_d from Eq.

(2-7). Overall we can estimate the relation between the subwavelength variation of the half-observation aperture-width and the dark-line pattern shift in linear form

$$\Delta x_d \cong -\frac{m\lambda z}{4a_0^2} \Delta a. \quad (2-13)$$



2.3.2 Simulation verification with subwavelength variation

To verify the feasibility of the relationship in Eq. (2-7) and (2-13) in detail, we carried out numerical evaluation for the variation of the first dark-line, while the observation aperture varying in subwavelength scale. In the case where the wavelength of the incident light was 632.8 nm , the detector was at a distance of 100 mm from the aperture, and the half aperture width along the x direction was $10\ \mu\text{m}$; the results are shown in the lighter lines in Fig. 2-6. The analytical result is depicted using a solid line, while the first-order approximation is shown with a dotted

line. The shifting of the diffraction pattern, associated with subwavelength variation, had good linear correlation and was magnified about 300 times. In this case, when the aperture variation was under $0.5 \mu m$, the inaccuracy of the first order approximation was under 5%. Taking the second order approximation, the inaccuracy would be less than 0.5%. Meanwhile, a direct numerical examination based on the Fraunhofer approximation ^[22], i.e., using the Fraunhofer diffraction integral, was used to evaluate the dark line position shift; this is shown with hollow triangular symbols. The diffraction pattern shift, with the half observing aperture with 100nm variation, is shown in Figs. 2-7(a) and (b). The half observation aperture was $10 \mu m$ and the detector, with dimensions $100 \mu m$ and $100 \mu m$, was centered at the first order dark-line position at a distance of $100 mm$ from the aperture. The pattern shift was $31.82 \mu m$, considering the subwavelength variation of the aperture was magnified about 300 times.

Again, for a comparison of section 2.3.1, the numerical evaluation of observing interference pattern with an embedded aperture are shown in Fig. 2-6 in the thicker lines. The numerical result from Eq. (2-11) is shown with a solid line, and the linear approximation result (Eq. (2-13)) is shown with a dotted line. The examination of the Fraunhofer approximation for the dark line position shift is shown with solid

triangular symbols. The diffraction pattern shift, caused by a 100nm variation of the half observing aperture, is shown in Figs. 2-7(c) and (d). The parameters used in the simulation were as follows: the half observation aperture was $10\ \mu\text{m}$; the detector (size: $100\ \mu\text{m} \times 100\ \mu\text{m}$) was centered at the first order of the dark-line position on the focal plane; and the focal plane was located at a distance of $100\ \text{mm}$ from the observing aperture. From the figures, one can see that the pattern shift was $15.49\ \mu\text{m}$; comparing the subwavelength variation of the aperture, the scale was magnified about 150 times.

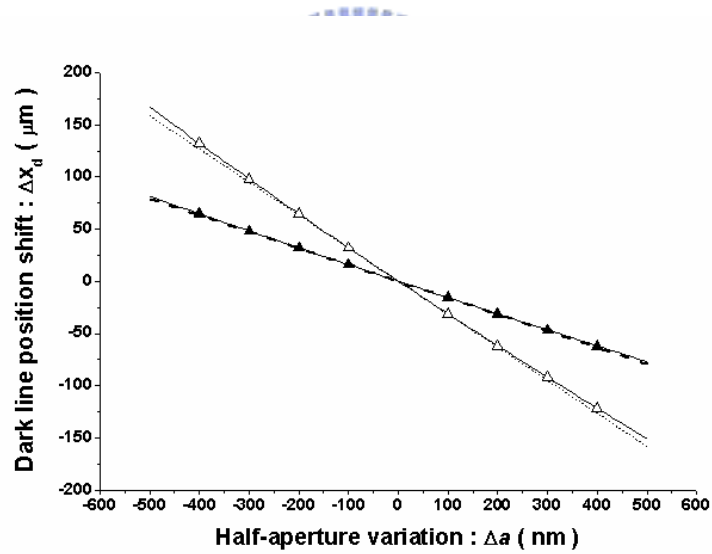


Fig. 2-6. The dark-line position shift versus the half aperture variation. The thicker line denotes the interferometer configuration, while the lighter line denotes the single aperture.

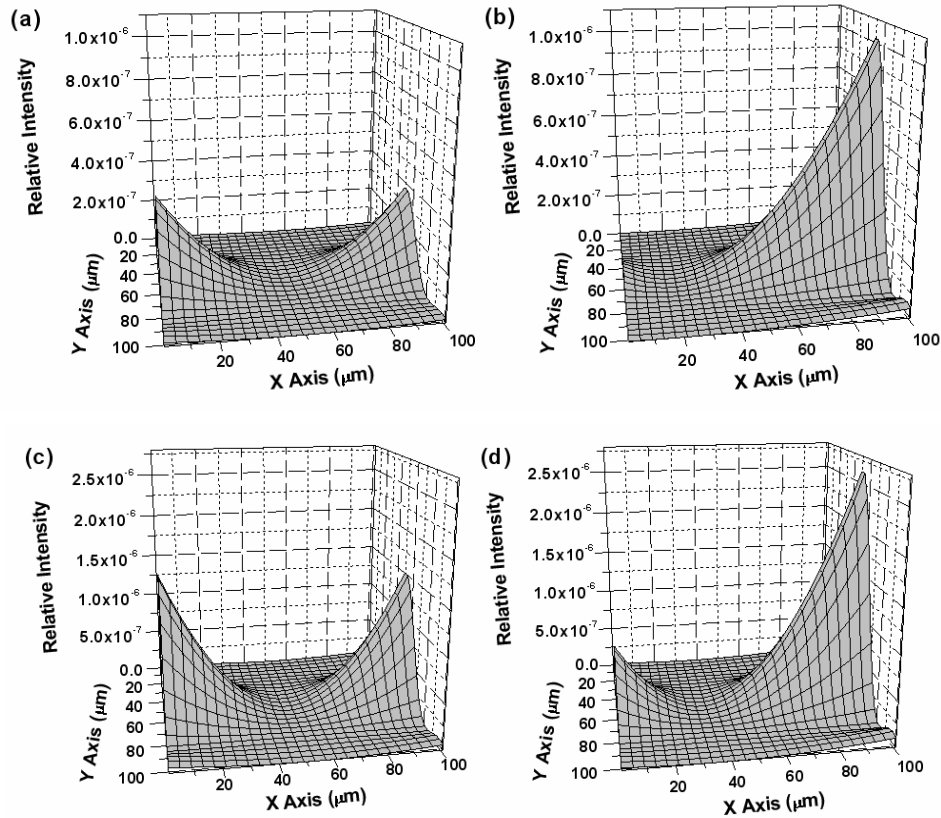
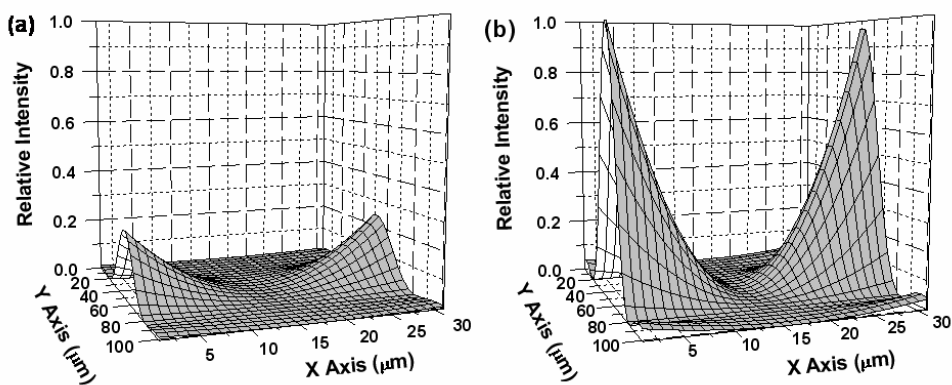


Fig. 2-7. The diffraction patterns before and after 100nm half aperture variation in two different situations. Directly detected method: (a) and (b); embedded-aperture interferometer configuration: (c) and (d).

2.3.3 Discussion on contrast influence in pattern measurement

The shifting of the diffraction pattern associated with subwavelength variation held a good linear correlation; however, under embedded-aperture interferometer configuration, the scale was magnified about 150 times, which is only half of the directly detected method. The shifting amount of the dark line, however, is not the only factor in taking a good measurement. Contrast of the diffraction pattern is also

crucial in detecting the signal. To demonstrate the influence of the contrast, we first calculated the intensity difference between the maximum and the minimum diffraction patterns within the area that was centered at the dark line position with a finite width; this was $30\ \mu\text{m}$, for both cases. We then normalized the intensity difference; the results are shown in Figs. 2-8 (a) and (b). The parameters used in the simulation were as follows: the half observing aperture was $10\ \mu\text{m}$; the detector was $30\ \mu\text{m} \times 100\ \mu\text{m}$ and was centered at the first order dark-line position on the focal plane; and the focal plane was located at a distance of $100\ \text{mm}$ from the observing aperture. The cross-section along the x axis of the first dark-line of the two cases is shown in Fig. 2-8 (c). It is obvious that the diffraction pattern of the embedded-aperture interferometer configuration is sharper than that of directly detected method, which implies that it is easier to confirm the detection of subwavelength variation, using the embedded-aperture interferometer configuration.



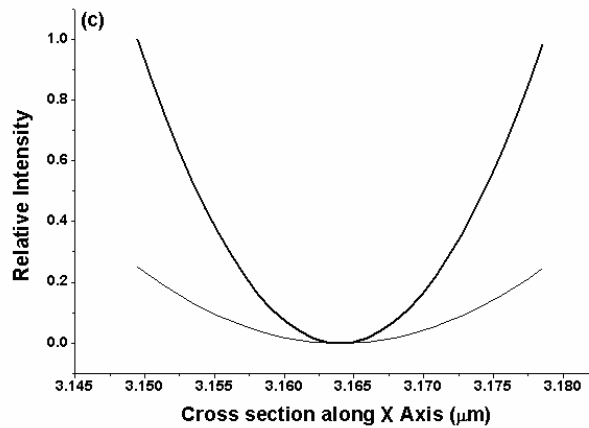


Fig. 2-8. The diffraction patterns centered at the first dark-line position: (a) directly detected method and (b) embedded-aperture interferometer configuration. (c): the cross sections along the X axis of (a) and (b), where the thicker line represents the embedded-aperture interferometer configuration and the lighter line represents the directly detected method.



2.4 Summary

In summary, it is shown that 1-D subwavelength signature of diffraction structure can be retrieved from the far-field characterization, such as irradiance and diffraction pattern. The 1-D dynamic subwavelength variation signature of a slit and a rectangular aperture is shown to be determinable from its far-field irradiance with a precision of better than 1 nm . Another feasible method of detecting subwavelength variation with diffraction pattern variation was also proposed. The variation of the subwavelength scale was verified contained in dark-line pattern shift and was

enlarged in an order about hundred times to be easily measured in the far-field.

Form the results of this chapter, it implies the possibility to extract much useful information, such as an object's thermal characteristic, vibration, deformation and others in the precision of *subwavelength scales*, form only far-field optical measurement.



Chapter 3

Enhancement of detection sensitivity of 1-D subwavelength variation measurement

3.1 Introduction

In the chapter 2, a scheme to retrieve the dynamic signature of the subwavelength variation from far-field irradiance with an appreciable quantity-derivative intensity with a precision of better than 1 nm was proposed. However, while measuring the structure variation in subwavelength scale, what we retrieved in the far-field is usually a weak optical signal and hence, it is a critical issue to enhance the detection sensitivity of the measurement. Therefore, effective measurement methodologies must be developed to retrieve subwavelength variation from far-field measurement, with a higher sensitivity. The enhancement of detection sensitivity is certainly possible to simply increase the light power that is transmitted through the test sample. However, in most situations, the test sample may suffer saturation and/or damage; hence, incident power must be limited. This means that enhancing detection sensitivity, via a direct increase of the incident power, simply may not work.

In this chapter, two embedded-aperture interferometer configurations were proposed, which could enhance the detection sensitivity of 1-D subwavelength variation measurement of a rectangular aperture with arbitrary aperture width ^[23,24]. In these configurations, an aperture (named the reference aperture) was posited symmetrically or asymmetrically relative to the aperture with the subwavelength variation was to be identified (named the test aperture). In symmetrical configuration, to enhance the detection sensitivity at any specific detection width, we have to modify the configuration and width size of the reference aperture. In asymmetrical configuration, the detection sensitivity could be enhanced at any specific detection width by only shifting the relative position of the reference aperture with fixed width size. On the other hand, with these two embedded-aperture interferometer configurations, the detection sensitivity is directly in proportion to the power of the reference beam. By increasing the power of the light beam transmitting through the reference aperture, detection sensitivity can be increased to a desired order without damaging the test sample owing to increase the incident power on the test aperture.

3.2 Symmetrically-embedded-aperture interferometer

3.2.1 Basic formalism and general features

Although it is not necessary to be limited to one specific interferometer configuration,

for simplicity, we have demonstrated a typical scheme. The proposed configuration, which is similar to the Mach-Zehnder Interferometer structure, is shown in Fig. 3-1. A common Mach-Zehnder interferometer was used, but with an embedded aperture, for which the associated subwavelength variation can be detected. In addition, another aperture was embedded for reference and optimization control.

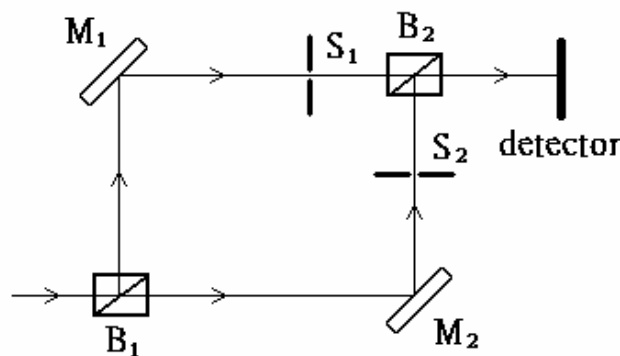


Fig. 3-1. Schematic diagram of interferometer configuration.

To be specific, a monochromatic plane wave of amplitude A and a wavelength λ was assumed to be orthogonally illuminated on a beam splitter B_1 . The beam was split into two after passing through the beam splitter. One beam was reflected by a mirror M_1 , and passed through a rectangular observation aperture S_1 , with dimensions $2a$ and $2b$. Another beam was reflected by mirror M_2 , and passed through another rectangular embedded aperture S_2 , whose dimensions were $2a'$ and $2b$. (For simplicity, we set the two apertures to be different in one direction only.)

Then the two beams were passed through another beam splitter B_2 and recombined into one beam. The diffracted intensity was collected over a rectangular detector. The detector was with dimensions $2X$ and $2Y$ centered at the beam width, and was positioned at a path distance z away from each aperture.

In the far field region, the diffraction field is the Fourier transform of the transmission function. The transmission functions of the two apertures are: $t_{s1} = \text{rect}\left(\frac{\varepsilon}{2a}\right)\text{rect}\left(\frac{\eta}{2b}\right)$ and $t_{s2} = \text{rect}\left(\frac{\varepsilon}{2a'}\right)\text{rect}\left(\frac{\eta}{2b}\right)$ where *rect* is the rectangle function. The diffraction optical fields of the two beams are

$$U_1 = A \frac{\exp\left(jkz + j\frac{\pi}{\lambda z}(x^2 + y^2)\right)}{j\lambda z} 4ab \text{sinc}(kax/z) \text{sinc}(kby/z) \quad (3-1)$$

and

$$U_2 = A \frac{\exp\left(jkz + j\frac{\pi}{\lambda z}(x^2 + y^2)\right)}{j\lambda z} 4a'b \text{sinc}(ka'x/z) \text{sinc}(kby/z) \quad (3-2)$$

, where k is the wave number, $j = \sqrt{-1}$, and *sinc* is used to denote the sinc function. The interference intensity distribution of these two beams on the detector is

$$I(x, y) = |U_1 + U_2|^2 = \frac{16A^2}{(\lambda z)^2} \frac{\text{sinc}^2(kby/z)}{(ky/z)^2} \left[\frac{\text{sinc}^2(kax/z)}{(kx/z)^2} + \frac{\text{sinc}^2(ka'x/z)}{(kx/z)^2} + 2 \frac{\text{sinc}(kax/z)\text{sinc}(ka'x/z)}{(kx/z)^2} \right] \quad (3-3)$$

The overall power P_z , flowing through the detector is

$$\begin{aligned}
P_z &= \int_{-x}^x \int_{-y}^y I(x, y) dx dy \\
&= \frac{16A^2}{(\lambda z)^2} \left[\int_{-y}^y \frac{\sin^2(kby/z)}{(ky/z)^2} dy \right] \left[\int_{-x}^x \frac{\sin^2(kax/z)}{(kx/z)^2} dx + \int_{-x}^x \frac{\sin^2(ka'x/z)}{(kx/z)^2} dx \right. \\
&\quad \left. + 2 \int_{-x}^x \frac{\sin(kax/z) \sin(ka'x/z)}{(kx/z)^2} dx \right] \quad (3-4)
\end{aligned}$$

Unlike the previous case of the non-interferometer approach mentioned in the chapter 2, an additional term are associated with the half observation aperture width a . In other words, with appropriate arrangement, it is possible to increase the sensitivity of the overall power variation with the observation aperture width.

To quantify the sensitivity, we first followed Ref. ^[19] and used derivative intensity $f_a = \frac{dP_z}{da}$. The derivative intensity can be deduced by using Leibniz's rule, resulting in

$$\begin{aligned}
f_a &= \frac{16A^2}{(\lambda z)^2} \times \frac{2zb}{k} \left[Si\left(\frac{2kbY}{z}\right) - \frac{\sin^2(kbY/z)}{(kbY/z)^2} \right] \\
&\quad \times \frac{2z}{k} \left[Si\left(\frac{2kaX}{z}\right) + \left(Si\left(\frac{k(a+a')X}{z}\right) - Si\left(\frac{k(a-a')X}{z}\right) \right) \right] \quad (3-5)
\end{aligned}$$

where Si denotes the sine-integral function.

To determine the maximum derivative intensity, the optimized enhancement of the sensitivity of the observed subwavelength variation was specified at half aperture width a . With two times the partial derivative with respect to half detector width X , the optimized condition was determinable. Within the proposed interferometer

configuration, the optimization condition required the half embedded aperture width a' of the reference beam and half detector width X to satisfy:

$$\begin{cases} a' > a \\ k(a + a')X / z = (2m_1 + 1)\pi \\ k(a - a')X / z = (2m_2 + 1)\pi \end{cases}, \quad (3-6)$$

where m_1 and m_2 are positive integer numbers. The result of $kaX / z = \pi$ and $ka'X / z = 2\pi$, by which Eq. (3-6) is fulfilled, is shown in Fig. 3-2.

3.2.2 Simulation verification and discussion

As a numerical demonstration, a half aperture width, $50 \mu m$, was considered. Meanwhile, a common light-source, the He-Ne laser, in which the wavelength is 632.8 nm , was used. The detector was at a distance of 100 mm from the aperture, the half detector width was $632.8 \mu m$, and the optimized reference beam half width was $100 \mu m$. We first considered the condition with the same size of detector. As shown in Fig. 3-2(a), with the interferometer configuration (thick solid line), the overall power variation on the detector was enhanced to 3.5 times that of the directly detected method (dotted line). Even when the detector for the directly detected method was optimized (thin solid line) by modifying the detector width ^[19], the sensitivity with the embedded-aperture interferometer configuration was still substantially (about 2.7 times) more than that of the directly detected method with optimized detector, as shown in Fig. 2(a).

A different observation aperture size did not affect the conclusion, as shown below.

In figures 3-2(b) and (c), the maximum sensitivity observation half aperture widths were optimized at $100\ \mu\text{m}$ and $150\ \mu\text{m}$, respectively. When the sensitivity of observation needs to be maximized, the embedded-aperture width can make twice as the observation aperture, and the detector size can be different for optimization.

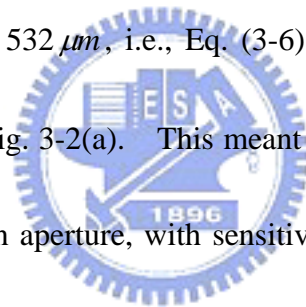
Re-setting for different wavelengths is straightforward, and sensitivity enhancement is always available. If the incident wavelength was changed, such as to 532nm , the

half detector width varied to $532\ \mu\text{m}$, i.e., Eq. (3-6) was satisfied; we obtained the same result as shown in the Fig. 3-2(a). This meant that it is possible to retrieve the

subwavelength variation of an aperture, with sensitivity enlarged nearly three times, by adding an arm with an additional appropriate aperture and observing the

interference pattern in the far field. A different observation aperture size, or using a

different wavelength, did not affect the conclusion; optimization could be performed.



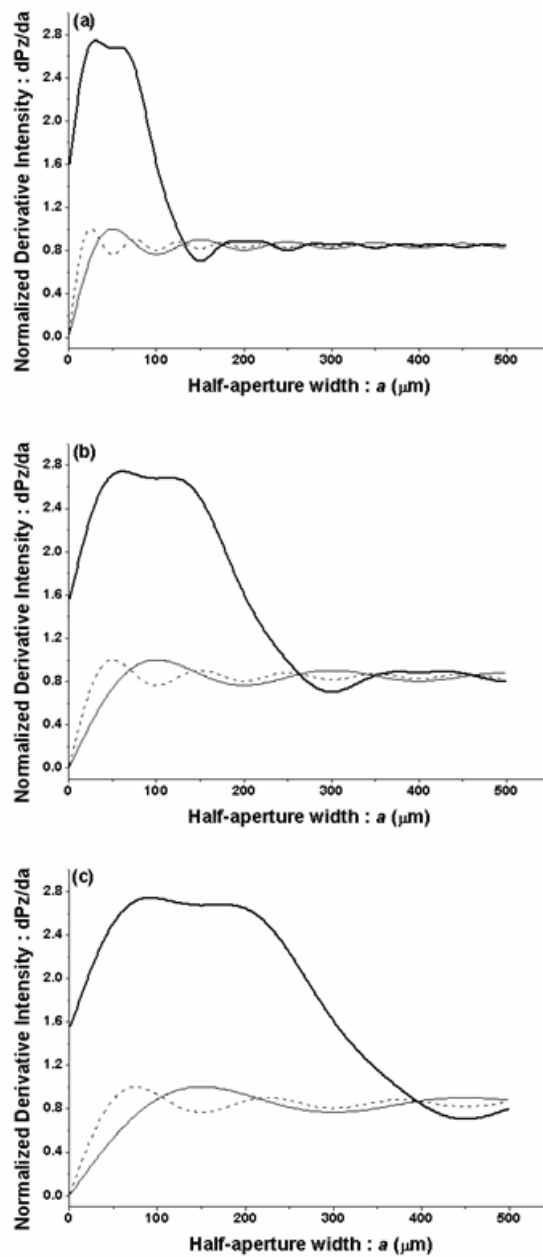
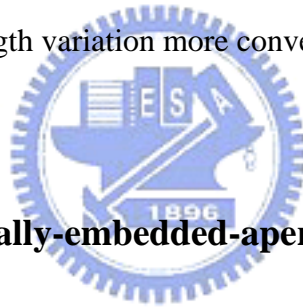


Fig. 3-2. Derivative intensity versus the half aperture width. The maximum sensitive observation half aperture was optimized at (a) $50 \mu m$, (b) $100 \mu m$, and (c) $150 \mu m$.

It should be noted that to enhance the detection sensitivity at a specified width of the observation aperture S_1 , a , the half detector width X and position of the detector, z , should be modified to satisfy the Eq. (3-6). Moreover, the width

of the reference aperture S_2 , a' , should also be modified with the width of the observation aperture S_1 , a . E.g., in the demonstration simulation $kaX/z = \pi$ and $ka'X/z = 2\pi$, i.e., the width of observation aperture S_2 , a' should be twice the the width of observation aperture S_1 , a . Though the proposed symmetrically-embedded-aperture interferometer can indeed to enhance the detection sensitivity of 1-D subwavelength variation measurement, it seems that it is not easy to implement in the realistic situation. In the next section, an tunable asymmetrically-embedded-aperture interferometer was proposed to the detection sensitivity of 1-D subwavelength variation more conveniently.



3.3 Tunable asymmetrically-embedded-aperture interferometer

3.3.1 Basic formalism and general features

The proposed configuration, which is similar to the Mach-Zehnder Interferometer structure, is shown in Fig. 3-3 (a). The test aperture, D_1 was associated with subwavelength variation to be identified. In addition, another embedded aperture, D_2 , which could be shifted, was embedded. The test-aperture, D_1 and the reference-aperture, D_2 were situated asymmetrically to the observing plane, as shown in Figs. 3-3 (b) and (c). Note that, if the detector position was not in the far-field region, then by introducing the focal lens against the apertures, as shown in

the dotted-circle in Figs. 3-3 (b) and (c), we could still observe the far-field diffraction pattern at the back focal plane, behind the lens.

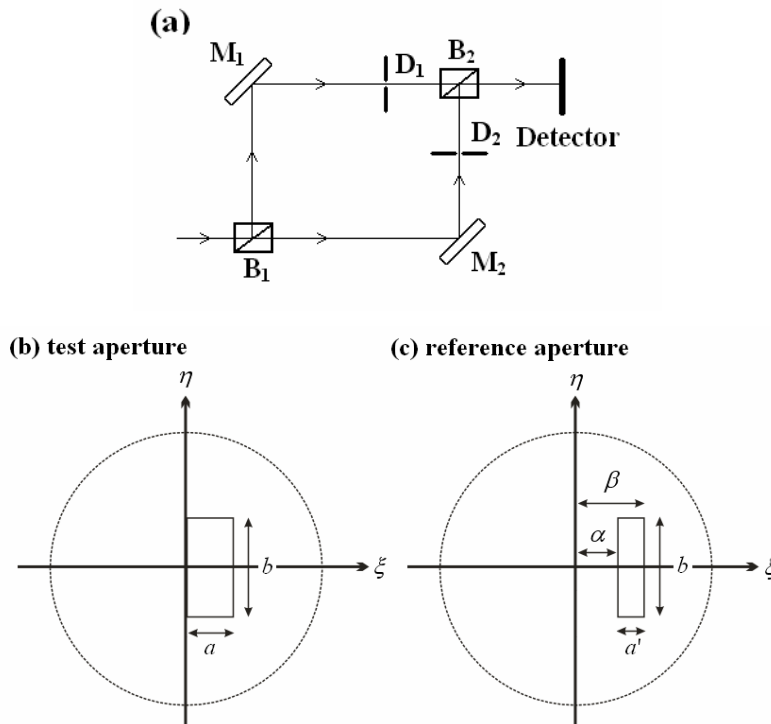


Fig. 3-3. (a) Schematic diagram of interferometer configuration. (b) The relative position of the detected-aperture. (c) The relative position of the embedded-aperture.

A monochromatic plane wave of amplitude A , and a wavelength λ , was assumed to be orthogonally illuminated on a beam splitter, B₁. The beam was split into two beams, after passing through B₁, each beam having a different amplitude, denoted by C_1 and C_2 ($C_1 + C_2 = A$). One beam was reflected by a mirror M₁, and passed through the test-aperture D₁, with dimensions a and b . The other beam, reflected by mirror M₂, passed through the reference-aperture D₂, whose dimensions

were a' and b , situated relative to the test-aperture with α along the ξ direction (see Figs. 3-3 (b) and (c)). After passing through another beam splitter B_2 , the two beams were recombined into one beam. The diffracted intensity was collected over a rectangular detector, with dimensions $2X$ and $2Y$, which were positioned at a path distance z away from each aperture. Considering the detector being situated at the Fraunhofer diffraction region, the diffraction optical field distribution is ^[25]

$$U(x, y) = \frac{e^{jkz} e^{j\frac{k}{2z}(x^2+y^2)}}{j\lambda z} \int_{-\infty}^{\infty} \int_{-\infty}^{\infty} U(\xi, \eta) \exp\left[-j\frac{2\pi}{\lambda z}(x\xi + y\eta)\right] d\xi d\eta, \quad (3-7)$$

where k is the wave number and $j = \sqrt{-1}$. The diffraction aperture is assumed to lie in the (ξ, η) plane and illuminate in the positive z direction. The symbol $U(\xi, \eta)$ represents the optical field behind the diffraction aperture. The optical field calculated was across the (x, y) plane, which is parallel to the (ξ, η) plane at a normal distance z . The diffraction optical fields of the two beams on the detector are

$$U_1(x, y) = \frac{e^{jkz} e^{j\frac{k}{2z}(x^2+y^2)}}{j\lambda z} C_1 \exp\left(-j\pi\frac{xa}{\lambda z}\right) \frac{\sin(\pi xa / \lambda z)}{\pi x / \lambda z} \frac{\sin(\pi yb / \lambda z)}{\pi y / \lambda z} \quad (3-8)$$

and

$$U_2(x, y) = \frac{e^{jkz} e^{j\frac{k}{2z}(x^2+y^2)}}{j\lambda z} C_2 \exp\left(-j\pi\frac{x(\beta - \alpha)}{\lambda z}\right) \frac{\sin[\pi x(\beta - \alpha) / \lambda z]}{\pi x / \lambda z} \frac{\sin(\pi yb / \lambda z)}{\pi y / \lambda z}. \quad (3-9)$$

The interference intensity distribution of the two beams on the detector is $I(x, y) = |U_1 + U_2|^2$. Because the intensity distributions of the two beams, in terms of y were the same, we defined the **intensity function** as $f_1(x)$, which only included the

influence of the x parameter of the interference intensity distribution, as follows:

$$f_I(x) = \left| C_1 \exp\left(-j\pi \frac{xa}{\lambda z}\right) \frac{\sin(\pi xa / \lambda z)}{\pi x / \lambda z} + C_2 \exp\left(-j\pi \frac{x(\beta - \alpha)}{\lambda z}\right) \frac{\sin[\pi x(\beta - \alpha) / \lambda z]}{\pi x / \lambda z} \right|^2. \quad (3-10)$$

Assume that the amplitude of the reference beam is γ times the beams transmitted through the test-aperture, i.e., $C_2 = \gamma C_1$ (γ is named as the **amplitude ratio**).

The intensity function can then be rewritten as

$$f_I(x) = |C_1|^2 \left[\frac{\sin^2(\pi xa / \lambda z)}{(\pi x / \lambda z)^2} + 2\gamma \frac{\sin(\pi xa / \lambda z)}{\pi x / \lambda z} \frac{\sin[\pi x(\beta - \alpha) / \lambda z]}{\pi x / \lambda z} \cos\left(\frac{\pi x}{\lambda z}(a - \alpha - \beta)\right) + \gamma^2 \frac{\sin^2[\pi x(\beta - \alpha) / \lambda z]}{(\pi x / \lambda z)^2} \right]. \quad (3-11)$$

The irradiance collected by the detector was denoted by symbol P_z , which can be

evaluated by $P_z = \int_{-X}^X \int_{-Y}^Y I(x, y) dx dy$. The detection sensitivity is proportional to the

far-field irradiance variation, with the change of observation aperture width, i.e., the

quantity dP_z / da . The **derivative intensity function** is defined as $f_a = \frac{\partial}{\partial a} \int_{-X}^X f_I(x) dx$,

which is proportional to the detection sensitivity. The detailed calculation gives us

$$f_a(a) = \frac{2z}{k} |C_1|^2 \left\{ 2Si\left(\frac{kaX}{z}\right) - \gamma \left[Si\left(\frac{k(a - \alpha)X}{z}\right) - Si\left(\frac{k(a - \beta)X}{z}\right) \right] \right\}. \quad (3-12)$$

Note that the first term in the derivative intensity function was same as that of the

directly detected case (i.e., without the embedded-aperture configuration), caused by

the variation of the test aperture without the reference aperture, as follows

$$f_{a1}(a) = \frac{4z}{k} |C_1|^2 Si\left(\frac{kax}{z}\right). \quad (3-13)$$

The second term in the derivative intensity function was raised from the adding the

asymmetric reference aperture, which introduces the reference beam to interfere with the detection beam; it follows that

$$f_{a_2}(a) = \frac{2z}{k} \gamma |C_1|^2 \left[Si\left(\frac{k(a-\alpha)x}{z}\right) - Si\left(\frac{k(a-\beta)x}{z}\right) \right], \quad (3-14)$$

named as the *interference function*.

The influence of detection sensitivity caused by embedded-aperture was discussed as follow. Assuming the amplitudes of the two beams are equal, i.e., $\gamma = 1$, the derivative intensities while embedded with different situations were shown in Fig. 3-4. In Figs. 3-4(a), (b) and (c) the widths of the reference apertures were fixed at $150 \mu m$, and the relative position α of the reference apertures were located at the right side, relative to the test aperture at $50 \mu m$, $150 \mu m$, and $250 \mu m$, respectively. In Figs. 3-4(d), (e), and (f), the relative positions of the reference apertures were fixed at $250 \mu m$, and the widths of the reference apertures were $50 \mu m$, $150 \mu m$, and $250 \mu m$, respectively. For every simulation in the paper, a rectangular detector, with dimensions $200 \mu m$ by $200 \mu m$, was positioned at a distance of $25 mm$ from each aperture. In addition, the widths of the two apertures lying along η -direction were both set to be $300 \mu m$. The analytical result of the derivative intensity of the proposed interferometer configuration is shown as a thick solid line, while the directly detected method (without interferometer mechanism) is shown as a

dotted line, for comparison. A direct numerical examination, based on the Fraunhofer diffraction integral, is shown with triangle symbols.

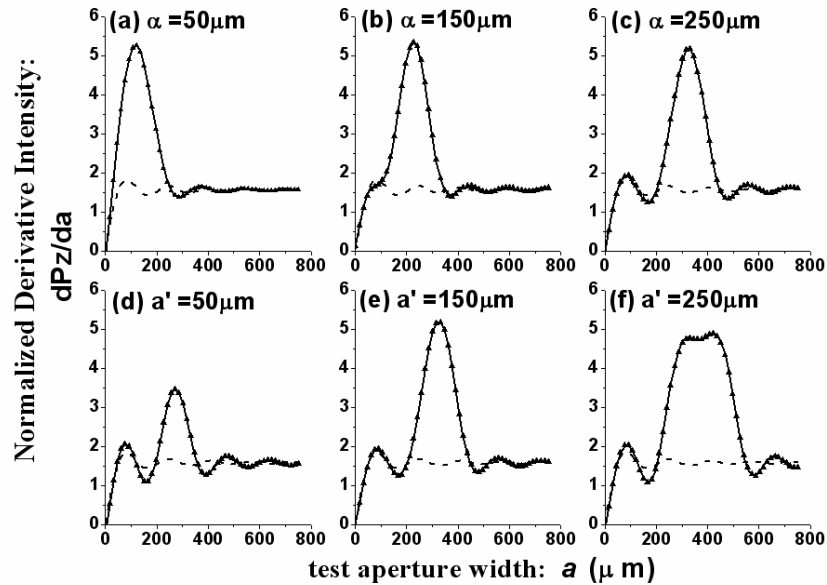


Fig. 3-4. Normalized derivative intensity versus the test aperture width. The reference aperture width: $150 \mu m$, relative position: (a) $50 \mu m$, (b) $150 \mu m$, and (c) $250 \mu m$. The relative position of the reference aperture: $250 \mu m$, with width: (d) $50 \mu m$, (e) $150 \mu m$, and (f) $250 \mu m$.

Three unique features can be identified from Fig. 3-4: (1) the form of the derivative intensity function is related to the reference aperture width, a' ; (2) the peak position of the derivative intensity function is relative to the position of the reference aperture, α ; and (3) we can see that by using a reference aperture, situated asymmetrically to the test aperture, as the reference beam for interference with the optical field of the test aperture, an additional peak in the derivative intensity function can be identified, i.e., *the detection sensitivity of measuring 1-D subwavelength*

variation of test-aperture was enhanced at the additional peak position of the derivative intensity function. In other words, shifting the reference aperture could enhance the detection sensitivity of any specific test aperture. To optimize the detection sensitivity at the specific test aperture width, we had to discuss the relationship between the reference aperture width a' , and the form of the derivative intensity function, as well as the relationship between the relative position of the reference aperture α and the peak of the derivative intensity function.

3.3.2 Detection sensitivity optimization

The detection sensitivity is directly proportional to the value of derivative intensity function, $f_a(a)$. Hence, we want to find the condition of the reference aperture that could optimize the detection sensitivity to have a maximum peak value at any specific test aperture width, a_0 . While both the detector width and the detector position were fixed, the first term of the derivative intensity function, $f_{a1}(a)$, was a function with stationary form with respect to the test aperture width a . The second term of the derivative intensity function, $f_{a2}(a)$, was linear independent with the function $f_{a1}(a)$, which was introduced by adding the reference aperture. Actually, the peak of the derivative intensity function was introduced by $f_{a2}(a)$. The interference function was made up of two sine-integral functions. Sine-integral

functions have such property that $Si(-x) = -Si(x)$; the maximum of the sine-integral function occurred at $x = \pi$, i.e. $Si(\pi) = 1$. The interference function can be rewritten as:

$$f_{a_2}(a) = \frac{2z}{k} \gamma |C_1|^2 \left[Si\left(\frac{k(a-\alpha)x}{z}\right) + Si\left(\frac{k(\beta-a)x}{z}\right) \right]. \quad (3-9)$$

To maximize the interference function at the specific detected-aperture width a_0 , the following relations must be satisfied:

$$\begin{cases} \frac{k(a_0 - \alpha)x}{z} = \pi \\ \frac{k(\beta - a_0)x}{z} = \pi \end{cases}. \quad (3-15)$$

Solving Eq. (3-15), the optimized condition, maximizing the detection sensitivity at the specified detected-aperture width a_0 was derived, i.e., the relative position of the reference aperture α , and the reference aperture width a' , which must satisfy:

$$\begin{cases} \alpha = a_0 - \lambda z / 2X \\ a' = \beta - \alpha = \lambda z / X \end{cases}. \quad (3-16)$$

The analytical and numerical demonstrations are shown in Fig. 3-5. The detection sensitivities were separately optimized, at three different test aperture widths a_0 , i.e., $100 \mu m$, $300 \mu m$, and $500 \mu m$. In these cases, the widths of the reference apertures a were fixed at $158.2 \mu m$, and the relative positions of the reference apertures α were $20.9 \mu m$, $220.9 \mu m$, and $420.9 \mu m$, respectively. In other words, in the measurement of the subwavelength variation of the aperture width, with the measurement of far-field irradiance variation, *by simply shifting the reference*

aperture, we could optimize the detection sensitivity at any test aperture width. It should be noted that by using optimized width of the reference aperture could let the derivative intensity having a maximum peak value; using different reference aperture widths may change the width of the derivative intensity and cause the peak value of derivative intensity function to decrease.

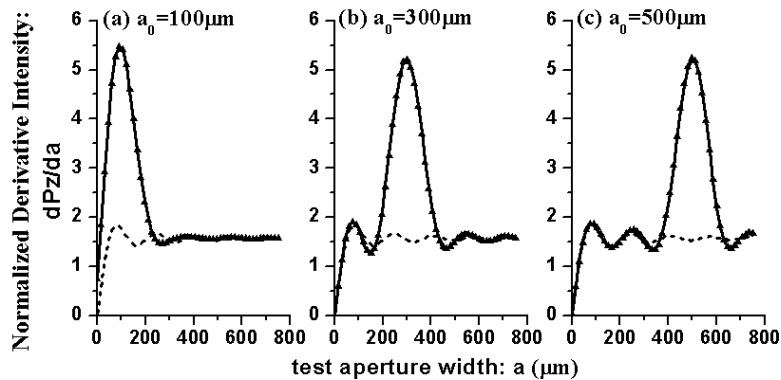


Fig. 3-5. Normalized derivative intensity versus the test aperture width. The maximum sensitive detected-aperture width was optimized at (a) $100 \mu m$, (b) $300 \mu m$, and (c) $500 \mu m$.

3.3.3 Discussion

Some properties of the proposed embedded-aperture interferometer will be discussed in this section. First, it is worthwhile to note that, in our proposed configuration, the detection sensitivity can be tuned to a desired order by only increasing the reference beam power. For example, the detection sensitivities were

optimized at the test aperture width $a_0 = 300\mu\text{m}$, with the amplitude ratios $\gamma = 1$ and $\gamma = 5$; the results are shown in Figs. 3-6(a), and (b), respectively.

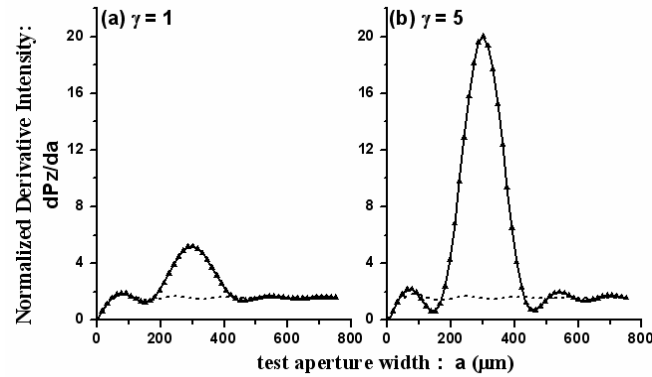
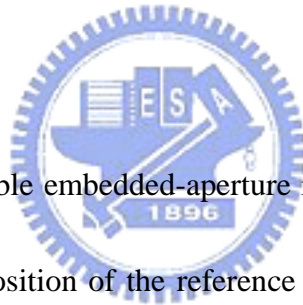
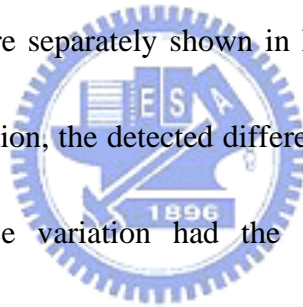


Fig. 3-6. Normalized derivative intensity versus the test aperture width with an amplitude ratio: (a) $\gamma = 1$, and (b) $\gamma = 5$.



Besides, in the proposed tunable embedded-aperture interferometer configuration, by simply shifting the relative position of the reference aperture, we could enhance the detection sensitivity of test aperture with arbitrary aperture width. Why does the derivative intensity could be enhanced by shifting the reference aperture, so do the detection sensitivity? The reason is that the action of interference of two beams rearranged the diffraction intensity distribution on the detector. The optimized condition of the reference aperture allowed the trend of the additional irradiance variation, introduced by the reference aperture on the whole detector, to be the same and the maximum. To illustrate the action of optimization by shifting the reference aperture, three different situations were analyzed. First, a reference aperture was

situated so that it satisfied the optimization condition Eq. (3-16), i.e., the relative position of the reference aperture was $70.9 \mu\text{m}$ and the width of the reference aperture was $158.2 \mu\text{m}$. Second, the reference aperture was shifted to a non-optimized relative position of $150 \mu\text{m}$. Finally, the reference aperture was shifted to a non-optimized relative position of $250 \mu\text{m}$. The difference in intensity, dI/da , with the detector at the width of the test aperture being $150 \mu\text{m}$ for the three situations, are shown in Figs. 3-7(a), (b) and (c), respectively. The additional irradiance variations introduced by interference that compared to the directly detected case of the three situations are separately shown in Figs. 3-7(d), (e) and (f). Note that in the optimization condition, the detected difference in intensity was maximized and the additional irradiance variation had the same positive trend. In the non-optimized condition, the additional irradiance variation was did not have a positive trend, so the difference in intensity was less than the optimized intensities.



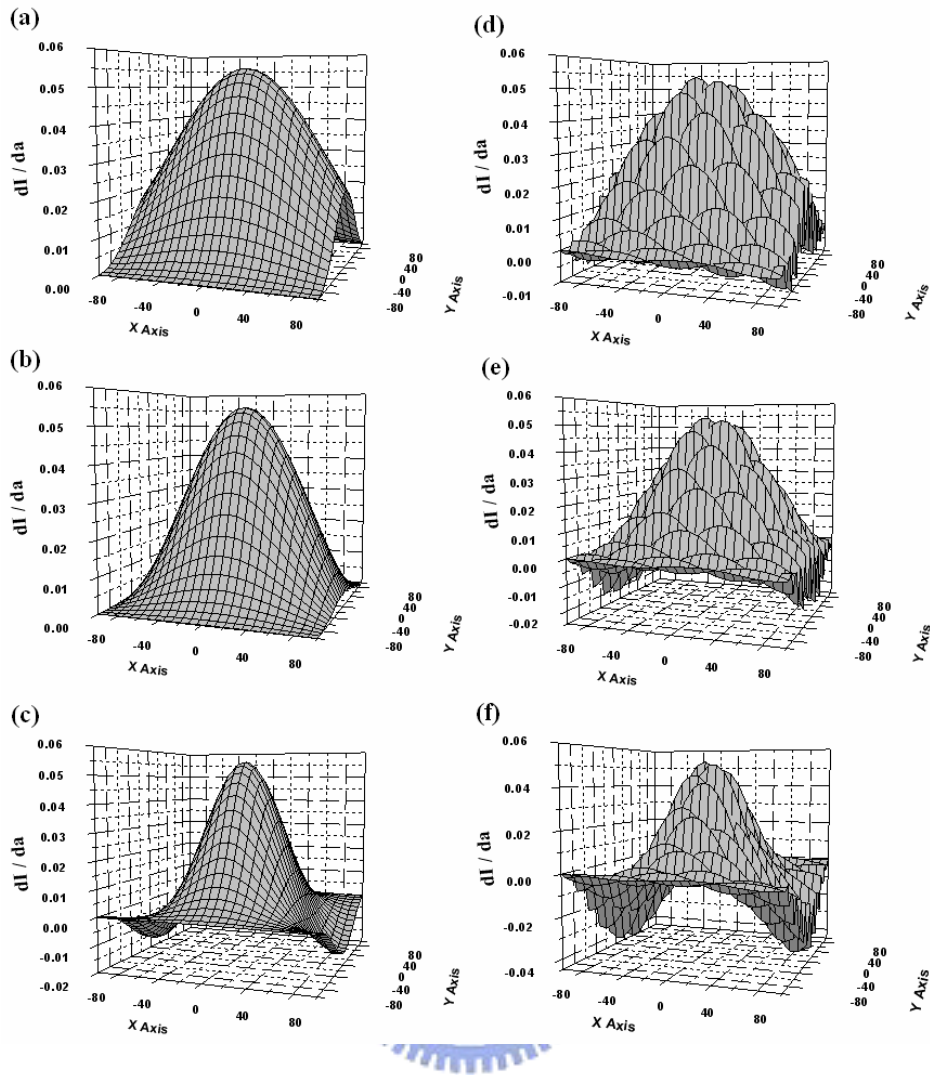
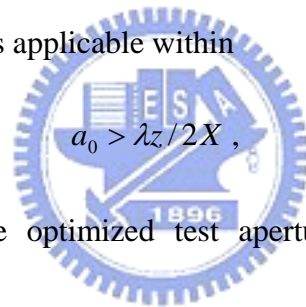


Fig. 3-7. The differences in intensity, dI/da , on the detector at the test-aperture width of $150\ \mu\text{m}$ are shown in Figs.3-7(a), (b) and (c). The additional irradiance variations, introduced by interference, compared to the directly detected cases of the three situations are shown in Figs. 3-7(d), (e) and (f). Optimized conditions: (a)(d), and non-optimized conditions : (b)(e) and (c)(f).

It is worthwhile to note that the optimization was processed by controlling the peak position of the interference term in the derivative intensity function, mainly by shifting the relative position of the reference aperture. In the region that

$a_0 > \lambda z / 2X$, the fluctuation of the first term in the derivative intensity function, i.e., f_{a1} , was not significant. Hence, the change in the additional peak position of the derivative position by the fluctuation of f_{a1} was small enough to be ignored. However, in the region of $a_0 < \lambda z / 2X$, the function f_{a1} was in the form of a linear increase and this change in the optimized peak position may be significant. Therefore, optimizing the peak position of the detection sensitivity, at a specific aperture width within $a_0 < \lambda z / 2X$, by shifting the relative position of the reference aperture will fail. In other words, the tunable asymmetrically-embedded-aperture interferometer configuration is applicable within



$$a_0 > \lambda z / 2X , \quad (3-17)$$

i.e., there is a limit on the optimized test aperture width a_0 . For instance, considering that $X = 100 \mu m$, $\lambda = 0.6328 \mu m$, and $z = 25 mm$, the limit on the optimized test aperture width is that it must be greater than $79.1 \mu m$. Nevertheless, with the enlargement of detector width and a shorter detector distance behind the apertures, the confinement of the optimized detected-aperture width a_0 can be decreased to the order of several times the wavelength, which is close to the limitation of the scalar diffraction theory. In other words, with a suitable arrangement of the configuration of the interferometer, the width limit of test sample can be ignored.

On the other hand, referring to Eq. (3-2) and (3-3), the effect of the relative position of the aperture to the system axis introduces the phase terms $\exp\left(-j\pi\frac{xa}{\lambda z}\right)$ and $\exp\left(-j\pi\frac{x(\beta-\alpha)}{\lambda z}\right)$. Shifting both the reference aperture and the test aperture to the left of $a/2$ does not change the result, i.e., the absolute positions of the two apertures are not important; however, the relative position of the reference aperture compared to the test aperture, controlled the optimization performance.

3.4 Summary

Considering in the situation that while the aperture are varying in subwavelength scale, the correspondence far-field optical signal might be weak to be detected in the far-field; and thus to develop the scheme to increase detection sensitivity is needed.

In this chapter, two embedded-aperture interferometer configurations were proposed to enhance the detection sensitivity of 1-D subwavelength variation measurement.

The tunable asymmetrically embedded-aperture interferometer configuration is more easily to be implemented in the real situation. In this configuration, a reference aperture was posited asymmetrically, relative to the test aperture, which exhibiting subwavelength variation. By only shifting the relative position of the reference aperture, the detection sensitivity of measuring the subwavelength variation in the far field can be enhanced to a desired value at any specific detection width.

Chapter 4

Deconvolution of 2-D subwavelength variation information

4.1 Introduction

The strategies of determination of 1-D dynamic signature of the subwavelength variation of the width of a rectangular aperture has been shown to be determinable from far-field irradiance measurement with a precision better than 1 nm or from the far-field pattern measurement are discussed in the chapter 2. The enhancement of the detection sensitivity of 1-D subwavelength signatures by using a tunable asymmetrically embedded-aperture interferometer configuration was discussed in the chapter 3. As shown in these results, these measurement schemes that retrieving of subwavelength dynamics variation are essentially one-dimensional. However, in more realistic situations, the structure may vary in two or three dimensions, and the characteristics of subwavelength variations contained in the far-field are coupled and thus will be difficult to separate. In this chapter, a multiple-detector measurement strategy, with a blind source separation method^[26], was proposed to decompose and characterize the two-dimensional dynamical signatures of subwavelength variations

from far-field optical measurements ²⁷.

4.2 Retrieving 2-D subwavelength variation characteristics with two-detector strategy

4.2.1 Basic formalism and general features

Two-detector system was proposed and was estimated to contain enough information to retrieve 2-D subwavelength variation information. To illustrate the basic idea of using multi-detector configuration to retrieve multi-dimension dynamical subwavelength variations, a two-detector measurement system was proposed to show how the characteristics of the two-dimensional signatures of subwavelength variation of a rectangular aperture could be retrieved.

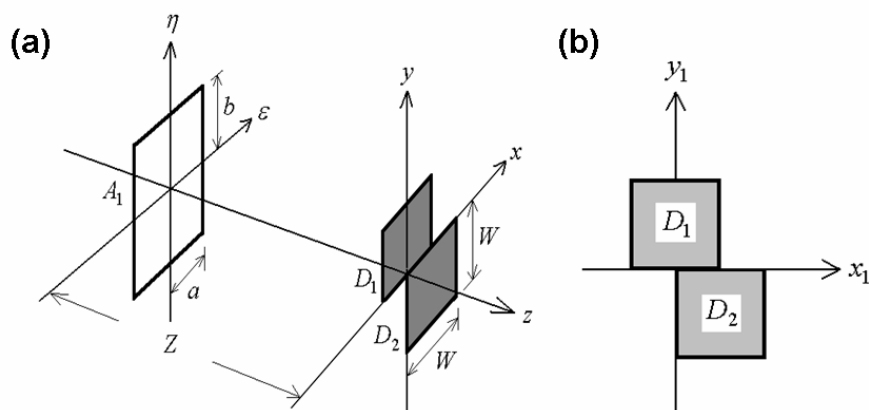


Fig. 4-1. Schematic diagrams of (a) a two-detector configuration, while (b) shows the relative positions of two detectors.

As shown in Fig. 4-1, a monochromatic plane wave of amplitude 1 and wavelength λ , is assumed to be orthogonally illuminated on the observing rectangular aperture A_1 , with dimension $2a \times 2b$. The dimensions of the two half widths of the rectangular aperture, a and b , are larger than several wavelengths, and each of them varied in time in subwavelength scale. Two detectors, D_1 and D_2 , with the same size $W \times W$ are positioned at different positions relative to the observing aperture A_1 , and are in the far-field region behind the observing rectangular aperture at a distance Z . The overall power collected by the two detectors are denoted as P_1 and P_2 . The relationship between the overall power variations: ΔP_1 , ΔP_2 , and the aperture width variations: Δa , Δb , can be written in the following matrix form:

$$\begin{bmatrix} \Delta P_1 \\ \Delta P_2 \end{bmatrix} = \begin{bmatrix} \partial P_1 / \partial a & \partial P_1 / \partial b \\ \partial P_2 / \partial a & \partial P_2 / \partial b \end{bmatrix} \begin{bmatrix} \Delta a \\ \Delta b \end{bmatrix}, \quad (4-1)$$

where $\partial P_1 / \partial a$, $\partial P_1 / \partial b$, $\partial P_2 / \partial a$ and $\partial P_2 / \partial b$ are named as *partial derivative intensity* of the overall power of the two detectors, and the definition of overall power variations and aperture width variations are: $\Delta P(t) = P(t + \Delta t) - P(t)$, $\Delta a(t) = a(t + \Delta t) - a(t)$, $\Delta b(t) = b(t + \Delta t) - b(t)$ (Δt is the time interval between every two measuring time point of detector). While the aperture varies in subwavelength scale, the variation of the quantity, partial derivative intensity, is small enough and thus can be assumed to be

time-independent as derivative intensity that illustrated in the chapter 2. As the relations shown in the Eq. (4-1), the overall power variations can be treated as linear mixtures of the aperture width variation, and thus the issue that retrieving the coupled signatures of the two-dimensional subwavelength variation can be treated as a classical blind source separation problem [22,28,29,30].

4.2.2 Time-delayed correlation methods

The classical blind signal separation problem could be illustrated in the Fig. 4-2.

The blind signal separation methods could recover the mixing independent source signals by the detected signal.

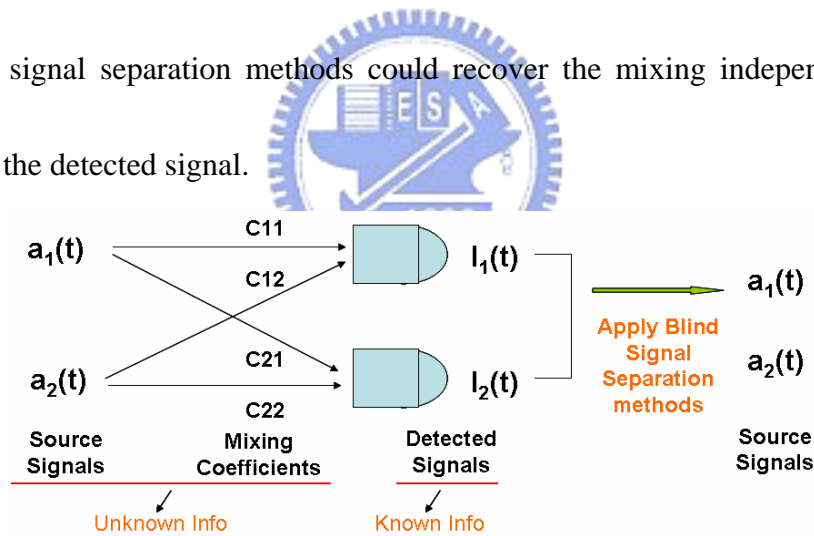


Fig. 4-2. Schematic diagrams of the blind signal separation problems

A less calculation complexity method of solving the blind signal separation problems, *time-delayed correlation method* [22] was applied to demonstrate the feasibility to separate the coupled multi-dimension far-field optical signal. This

method is summarized as follows: N statistically independent source signals, a_i ($i=1,2,\dots,N$), satisfying the condition, $\langle a_i(t)a_j(t') \rangle = K(t'-t)\delta_{ij}$, were mixed linearly in N detected signals, $I_i = \sum_j^N C_{ij}a_j$ ($i=1,2,\dots,N$), which were recorded by N detectors, where C_{ij} are the mixing coefficients. The key is to solve the $N(N+1)$ unknown variables, i.e., the mixing coefficients C_{ij} and the source signal strength $\lambda_i = K_i(0)$, by the measurements I_i . This method introduces the additional assumption that the mean value of the source signal is zero, $\langle a_i(t) \rangle = 0$, and constructs two matrices, the *symmetrical correlation matrix* $M_{ij} = \langle I_i(t)I_j(t) \rangle$ and the *time delayed correlation matrix* $\overline{M}_{ij} = \langle I_i(t)I_j(t+\tau) \rangle$, whose clear forms are $M_{ij} = \sum_l^N C_{il}C_{jl}\lambda_l$ and $\overline{M}_{ij} = \sum_l^N C_{il}C_{jl}\overline{\lambda}_l$. The mixing matrix C can diagonalize M and \overline{M} in such form that $C^{-1}M(C^T)^{-1} = \Lambda$ and $C^{-1}\overline{M}(C^T)^{-1} = \overline{\Lambda}$, where $\Lambda_{ij} = \lambda_i\delta_{ij}$ and $\overline{\Lambda}_{ij} = \overline{\lambda}_i\delta_{ij}$. Multiplying the matrix Λ by $\overline{\Lambda}^{-1}$, the blind signal separation problem becomes an eigenvalue problem where $(M\overline{M}^{-1})C = C(\Lambda\overline{\Lambda}^{-1})$. While solving the mixing coefficients C_{ij} , it could be easily adopted to solve the source signal. More detail could be founded in Appendix II.

4.2.3 Retrieving results and scaling issues

The feasibility of the proposed two-detector measurement could retrieve 2-D

subwavelength variation characteristics from measuring the coupled far-field optical information was demonstrated as follows. In our situation, we want to use the measurements that overall power variation of two detectors: ΔP_1 , ΔP_2 , to retrieve the aperture width subwavelength variations: Δa , Δb . Without loss of generality, the variation types of the observing aperture widths were set as: one dimension as random fluctuation, and the other dimension as quasi-periodic variations. The aperture width that varying in random fluctuation is specified by $a(t) = a_0 + \alpha \times \eta(t)$, where $\eta(t)$ is a random fluctuation with a value ranging from -1 to 1. The other aperture width that varying in quasi-periodic subwavelength variation is given by $b(t) = b_0 + \alpha \times \cos(2\sqrt{2}\pi ft) + \alpha \times \sin(2\sqrt{5}\pi ft)$. Here all amplitudes of variation α are set to 10 nm for simplicity, and the frequency of vibration f , is taken to be 100 Hz. The sampling rate of detection is 10 KHz, which is higher than the frequency of the vibration of the aperture widths. The half-width of the aperture a_0 , b_0 are both 50 μm . The widths of the detector W are all 100 μm ; and the detector is placed behind the aperture at a distance of 30 mm. A light source wavelength of 632.8 nm was used. The overall power variation of the two detectors: ΔP_1 and ΔP_2 , were evaluated numerically by scalar diffraction theory, and used to retrieve the subwavelength-scale width variation: Δa and Δb .

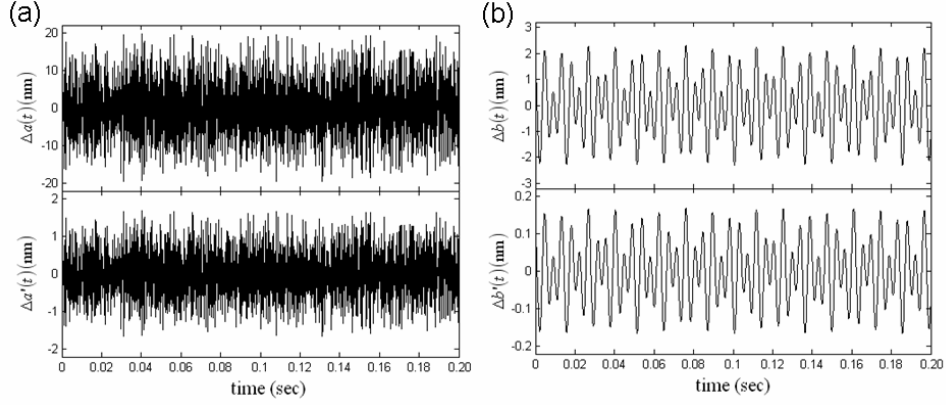


Fig. 4-3. The results of two-detector configuration. (a) the setting and retrieving aperture width variations: Δa and $\Delta a'$, and (b) the setting and retrieving aperture width variations: Δb and $\Delta b'$.

The retrieving results of the proposed two-detector measurement are shown in Fig. 4-3. The retrieving aperture width variations: $\Delta a'$ and $\Delta b'$ behave the same way as the simulation setting aperture width variations: Δa and Δb , but *in a different scale*, i.e., the characteristics of the subwavelength signatures of the aperture that the variation forms can indeed be retrieved by the proposed strategy, but variation strength can't. This is because that the eigenvectors are usually normalized to unity in the deconvolution method. But, in reality the mixed coefficients C_{ij} will not have to be that. As an example, for $N = 2$, the scaling effect can be shown in the matrix form as:

$$\begin{bmatrix} \Delta P_1 \\ \Delta P_2 \end{bmatrix} = \begin{bmatrix} \frac{\partial P_1}{\partial a} / \alpha_1 & \frac{\partial P_1}{\partial b} / \alpha_2 \\ \frac{\partial P_2}{\partial a} / \alpha_1 & \frac{\partial P_2}{\partial b} / \alpha_2 \end{bmatrix} \begin{bmatrix} \alpha_1 \Delta a \\ \alpha_2 \Delta b \end{bmatrix}, \quad (4-2)$$

where α_i ($i=1,2$) correspond to the scaling factors. What we retrieved is the scaled width variation: $\alpha_1\Delta a$, $\alpha_2\Delta b$, i.e., we can indeed retrieve the subwavelength variation type with the two-detector configuration, but with a wrong strength. One solution to determine the scaling exactly will be proposed in the next section.

4.3 Three-detector embedded-aperture interferometer configuration

A three-detector measurement configuration is proposed to retrieve the correct magnitude of 2-D subwavelength variations in this section.

4.3.1 Basic formalism and general features

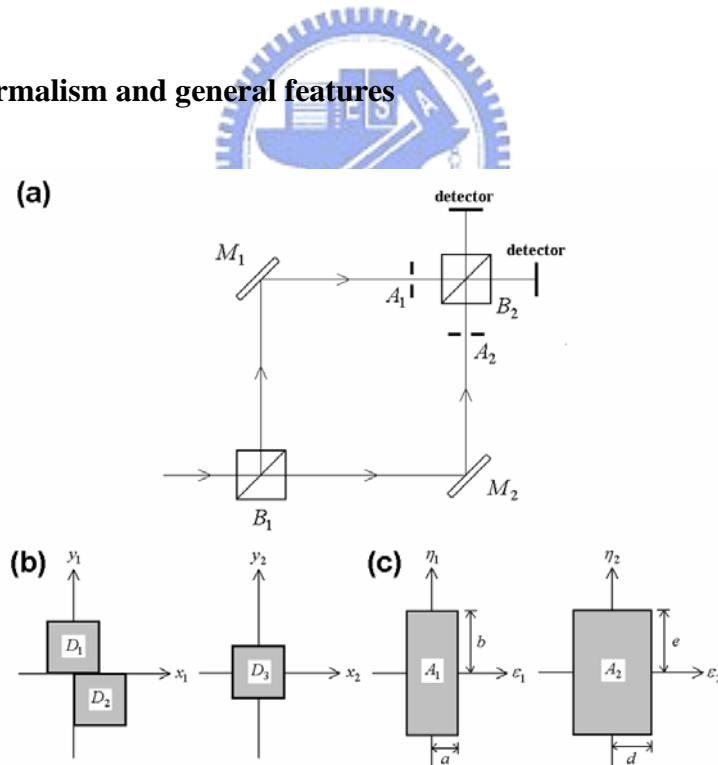


Fig. 4-4. Schematic diagrams of (a) an embedded-aperture three-detector interferometer while (b) shows the relative positions of the detectors. (c) Schematic diagram of the sizes of the two apertures.

Referring to Fig. 4-4, the proposed configuration of solution is an embedded-aperture interferometer configuration similar to the Mach-Zehnder Interferometer, but with one embedded aperture and three detectors. A monochromatic plane wave of a wavelength λ is assumed to be orthogonally illuminated on a beam splitter B_1 . The beam is split into two after passing through the beam splitter. One beam is reflected by a mirror M_1 , and passed through a rectangular observation aperture A_1 , with dimensions $2a \times 2b$. Another beam is reflected by a mirror M_2 , and passed through the introduced embedded aperture A_2 , which has a choosing fixed aperture width e that is to be extremely equal to the width of the observing aperture, b , and has the other aperture width d with an embedded varying form. Then the two beams are passed through another beam splitter B_2 to be recombined and further separated into two beams. The diffracted intensity is collected over three rectangular detectors with the same dimensions $W \times W$, which are positioned at a distance Z away from each aperture. It should be noted that the third detector D_3 is chosen to be positioned at a different location from the other two detectors to record additional information.

The relations of overall power variations: ΔP_1 , ΔP_2 , ΔP_3 , and the aperture width variations: Δa , Δb , Δd are as follows

$$\begin{bmatrix} \Delta P_1 \\ \Delta P_2 \\ \Delta P_3 \end{bmatrix} = \begin{bmatrix} \frac{\partial P_1}{\partial a} / \alpha_1 & \frac{\partial P_1}{\partial b} / \alpha_2 & \frac{\partial P_1}{\partial d} / \alpha_3 \\ \frac{\partial P_2}{\partial a} / \alpha_1 & \frac{\partial P_2}{\partial b} / \alpha_2 & \frac{\partial P_2}{\partial d} / \alpha_3 \\ \frac{\partial P_3}{\partial a} / \alpha_1 & \frac{\partial P_3}{\partial b} / \alpha_2 & \frac{\partial P_3}{\partial d} / \alpha_3 \end{bmatrix} \begin{bmatrix} \alpha_1 \Delta a \\ \alpha_2 \Delta b \\ \alpha_3 \Delta d \end{bmatrix}. \quad (4-3)$$

By using the time delayed correlation method, the scaled mixing coefficients and three scaled aperture width variations, $\alpha_1 \Delta a$, $\alpha_2 \Delta b$, and $\alpha_3 \Delta d$ can be deduced from the overall power variations ΔP_1 , ΔP_2 , and ΔP_3 as collected by the three detectors. Following the approaches similar to that in chapter 2 and 3, the partial derivative intensity of D_3 that position at a symmetric position could be derived as

follows:

$$\begin{aligned} \frac{\partial P_3}{\partial b} &= \frac{16}{\lambda^2 k Z} P_a(a, d, W/2) Si(kbW/Z) \\ \frac{\partial P_3}{\partial a} &= \frac{16}{\lambda^2 k Z} P_b(b, W/2) \{ Si(kaW/Z) + Si[k(a+d)W/2Z] - Si[k(a-d)W/2Z] \} \end{aligned}, \quad (4-4)$$

where k is the wave number, Si is the sine integral function, and the two functions $P_a(a, d, W/2) = \int_0^{W/2} \frac{[\sin(kax/Z) + \sin(kdx/Z)]^2}{(\pi x / \lambda Z)^2} dx$ and $P_b(b, W/2) = \int_0^{W/2} \frac{\sin^2(kby/Z)}{(\pi y / \lambda Z)^2} dy$ can be evaluated numerically. By comparing the partial derivative intensity of D_3 :

$\partial P_3 / \partial a$ and $\partial P_3 / \partial b$, to the retrieving elements of mixing matrix in Eq.(4-3), the scaling factor, α_1 and α_2 , can be easily solved and thus we can retrieve the aperture width subwavelength variations: Δa , Δb in a correct magnitude.

On the other hand, there is another advantage of introducing the embedded

aperture width variation Δd . In the time-delay correlation method, the retrieving signal error of is related to the choice of the parameter of time delay, τ . Taking the error between retrieving embedded-variation $\Delta d'(t)$ and embedded-variation $\Delta d(t)$ as a reference could help us to decide a proper time delay, τ . The inverse mean error of the retrieving embedded-variation $\Delta d(t)$ was defined as

$$\text{Inverse mean error} = 1/\langle |\Delta d'(t) - \Delta d(t)| \rangle. \quad (4-5)$$

It could be verified that with the use of higher inverse mean error can have a better retrieving result.



4.3.2 Simulation verification and Discussions

In this section, we provide the support evidence of our approach. The simulation setting of the observation aperture A_1 was the same as that in section 4.2.3. Without loss of generality, the width variation form of the embedded-aperture A_2 is chosen as a sine form, i.e., $d(t) = d_0 + \alpha \sin(2\pi ft)$. The half width of the embedded aperture is chosen as $70 \mu m$, and the amplitude of variation α is set to be 10 nm and the frequency of vibration is taken to be 100 Hz.

The retrieving results of the proposed three-detector configuration are shown in Fig. 4-5. The relation between the time delay, τ , to the inverse mean error of the retrieving embedded-signal variation $\Delta d(t)$ is shown in Fig. 4(a) and hence, the time

delay is chosen as 0.0294 sec, so as to have a higher performance. The errors, $\Delta a'(t) - \Delta a(t)$ and $\Delta b'(t) - \Delta b(t)$ are shown in Figs. 4(b) and (c) in thick lines, while the setting aperture width variations $\Delta a(t)$ and $\Delta b(t)$ are plotted in gray thin lines as a reference, and the error percentage, the ratio that the difference between exact setting and numerically retrieving value to the amplitude of the setting aperture width variations value, are plotted in the base portion. Referring to Fig. 4-5, one can see that with the three-detector embedded-aperture configuration, the subwavelength signatures can be retrieved in a good precision and the retrieving aperture width variations, $\Delta a'$ and $\Delta b'$ are with an error ratio below 1%.



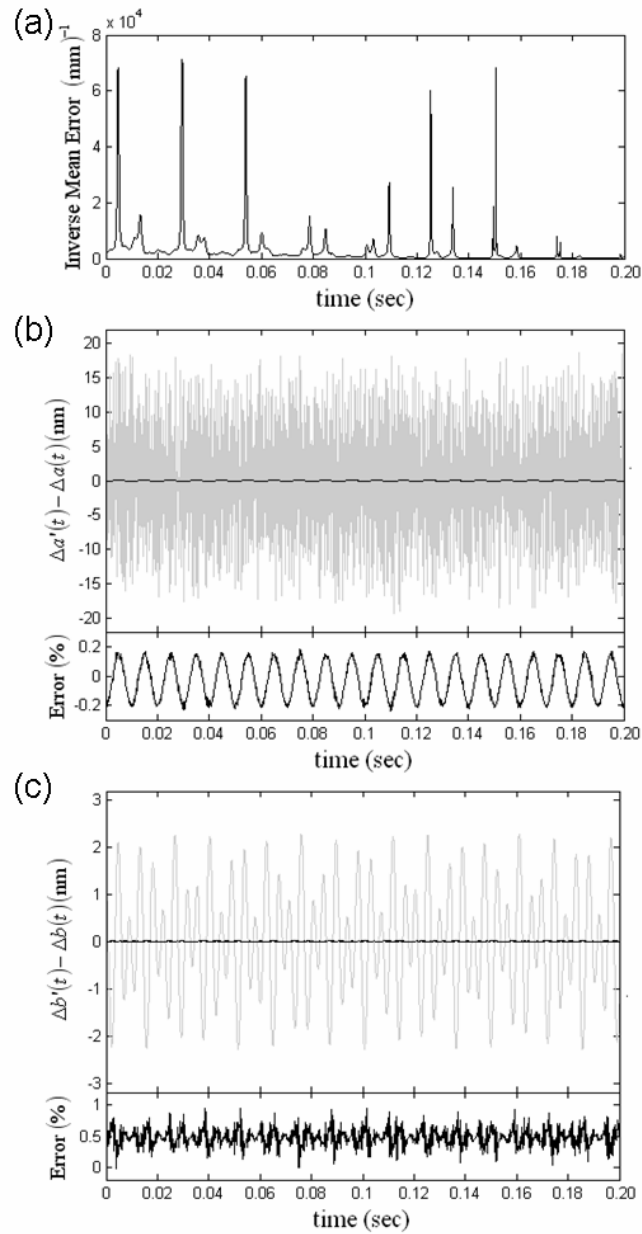


Fig. 4-5. (a): The inverse mean error of the retrieving embedded-aperture variation versus the time delay, τ . (b) the error and error percentage between setting and retrieving aperture width variations: Δa and $\Delta a'$, (c) the error and error percentage between setting and retrieving aperture width variations: Δb and $\Delta b'$.

There are two points that should be noted. First, the embedded variation of the

reference aperture, $\Delta d(t)$, is unnecessary to be in the subwavelength scale, but could be in a larger scale to be more easily to carry out. A larger half aperture width of $d_0 = 0.5mm$, that varies with a larger amplitude of $\alpha = 1\mu m$ can still be used to retrieve the two-dimension subwavelength with an acceptable error ratio below 3% signal. Secondly, a better result could be obtained with more recorded data. For example, in our simulation, 2000 recording data was used to achieve the maximum error ratio bellow 1%. But with 600 recording data can only have a best maximum error ratio of 1.94%.

4.4 Summary



While retrieving 1-D subwavelength-scale variation from far-field measurement has been demonstrated to be possible, we want to find approaches to retrieve subwavelength-scale variation toward more realistic situation. Thus, in this chapter, a rectangular aperture varying in 2-D with in subwavelength-scale has been discussed. A scheme to retrieve the coupled two-dimension subwavelength signatures by a three-detector embedded-aperture configuration accompanying time-delayed correlation method from far-field irradiance measurement was proposed. The precision of the proposed measurement was numerically verified could successfully characterize the two-dimensional dynamical signatures of subwavelength variations

information with error ratio below 1%.

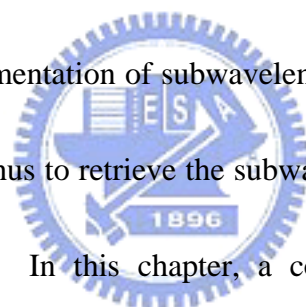


Chapter 5

1-D Marginal Roughness Measurement

5.1 Introduction

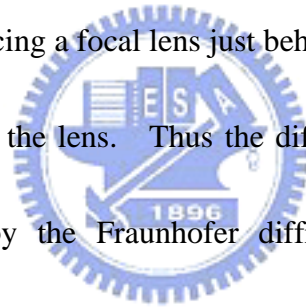
In the chapter 2 and chapter 4, it has been shown that the subwavelength temporal variation of a simple case, i.e., a 1-D and 2-D subwavelength-scale *temporal* variation can be retrieved from a far-field irradiance measurement. It is of interests to express the possible implementation of subwavelength spatial variation in terms of far-field characteristics, and thus to retrieve the subwavelength-scale *spatial* variation from far-field measurement. In this chapter, a conceptual construction will be proposed as an optical ruler, which could be used to identify the spatial *subwavelength scale* marginal-roughness variation from only far-field irradiance measurement.



5.2 Constructed-aperture roughness measurement system

Referring to Fig. 5-1, a constructed-aperture measurement system behaving as an optical ruler was proposed to retrieve the marginal roughness of the test sample. The diffraction aperture Σ was constructed by a slit-like aperture and the margin of the

test sample, where the width of the slit-like aperture along the η direction was denoted as b . A monochromatic plane wave of amplitude 1 and wavelength λ was assumed to be orthogonally illuminated onto the constructed aperture Σ . The margin of the test sample was situated relative to the straight margin of the slit-like aperture in a base width a_0 . The dimensions of a_0 and b were both above several wavelengths for satisfying the assumptions of the scalar diffraction theorem. The front view of the constructed aperture was shown in Fig. 5-1 (b). A detector with the size $W \times W$ was positioned behind the aperture Σ at a distance Z_0 in the far-field region, or by introducing a focal lens just behind the aperture Σ , situated the detector at the focal plane of the lens. Thus the diffraction pattern on the detector plane could be evaluated by the Fraunhofer diffraction. The overall power collected by the detector was denoted as P_z .



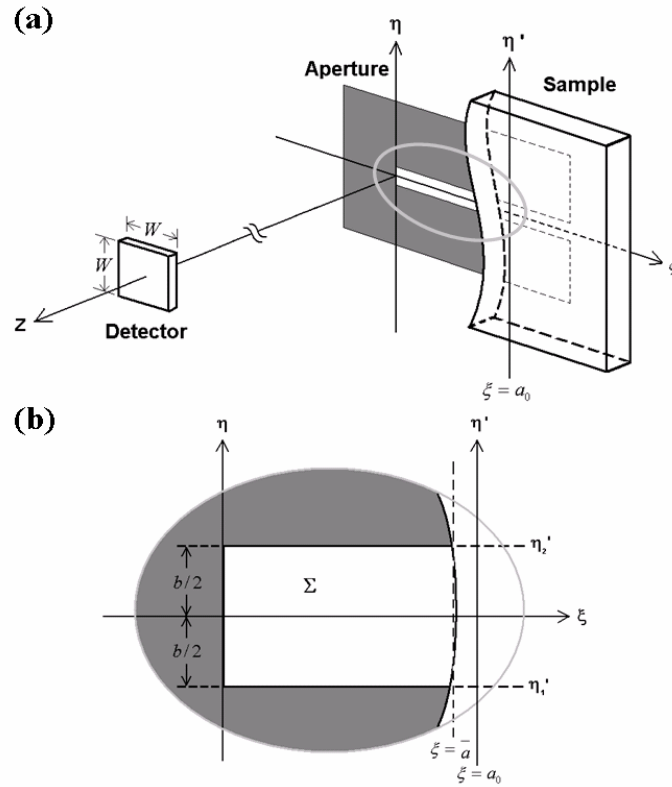


Fig. 5-1. Schematic diagrams of (a) constructed-aperture marginal roughness measurement system, (b) a front view of the constructed aperture of the system.

To illustrate the main idea of the proposed scheme, we recalled that in chapter 2, 1-D subwavelength temporal variation can be retrieved from a far-field irradiance measurement in a precision better than 1 nm by the following approximation, i.e.,

$$\Delta a \cong \Delta P_z / \left(\frac{dP_z}{da} \Big|_{a=a_0} \right). \quad (5-1)$$

In the proposed constructed-aperture measurement system, while the width deviation from the base width a_0 , Δa , of a rectangular aperture in a dimension $a_0 \times b$, was in a scale of subwavelength, the aperture width deviation Δa could be retrieved

from a physical parameter, i.e., the derivative intensity $\left. \frac{dP_z}{da} \right|_{a=a_0}$. ΔP_z is the deviation of the overall power comparing to that of the base width a_0 , $P_z(a_0)$, i.e. $\Delta P_z = P_z(a) - P_z(a_0)$. The key idea of the proposed measurement is that, while the width of the optical ruler b is small enough as compared to the spatial-variation scale of the marginal roughness T_d , the margin of the test sample could be estimated as a straight surface. The width of the constructed aperture (or say the averaging width) was denoted as \bar{a} , which could be retrieved by far-field irradiance measurement. The procedures are stated as below.



First, we need to derive the derivative intensity of an aperture varying in one-dimension with only one side, in a correspondence to the constructed measurement system here. It is for the reason that while measuring the marginal roughness, the test sample will be moved in the η direction. Because the marginal roughness is varied spatially from point to point, the width of the constructed aperture Σ , a , will be changed as the sample is moved. The constructed aperture will vary only on one side and the derivative intensity of measured power, dP_z/da , could be deduced following the same approaches as in chapter 2.

The exact form of the diffraction pattern on the detector U can be derived from

Fraunhofer diffraction, and the intensity is $|U|^2$. The overall power collected by the detector is the integration of the intensity over all the complete detector area, which is also the function of the varying aperture width a ,

$$P_z(a) = 4 \left(\frac{\lambda Z_0}{\pi} \right)^2 f_p(W/2, a) f_p(W/2, b), \quad (5-2)$$

where the function $f_p(X, a) = \int_0^X \frac{\sin^2[kax/2Z_0]}{x^2} dx = \frac{ka}{2Z_0} Si\left(\frac{kaX}{Z_0}\right) - \sin^2\left(\frac{kaX}{2Z_0}\right)/X$.

$k = 2\pi/\lambda$ is the wave number, and Si is the sine-integral function. The derivative intensity is the derivation of overall power P_z over the varying aperture width a , which can be derived as

$$\frac{dP_z}{da} = 8 \frac{Z_0}{k} f_p(W/2, b) Si\left(\frac{kaW}{2Z_0}\right). \quad (5-3)$$

The numerical value of the derivative intensity $\left. \frac{dP_z}{da} \right|_{a=a_0}$ can be evaluated from Eq.

(5-3), and can be substituted into Eq. (5-1) to retrieve the margin position of the test

sample as $\bar{a} = a_0 + \Delta a$.

5.3 Thickness effect of test sample

In section 5.2, the constructed aperture is estimated as an ideal planar aperture.

However, in a real situation, the test sample will have a thin thickness d inevitably.

As shown in the Fig. 5-2, the actual constructed aperture Σ' will have an inclination

angle, $\phi = \tan^{-1}(d/a_0)$, to the incident plane wave.

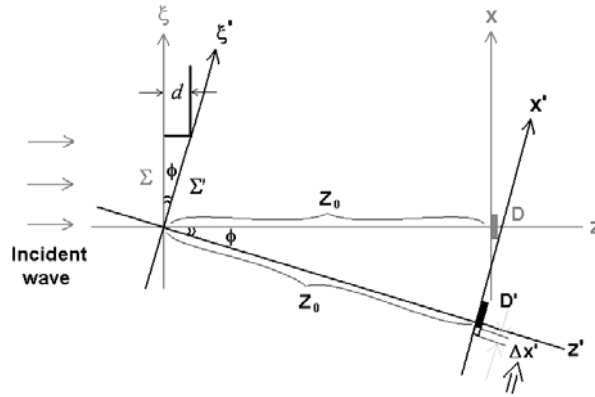


Fig. 5-2. Schematic diagram of a side view of the constructed-aperture marginal roughness measurement system.

The introducing power deviation from the thickness of the test sample cannot be neglected as comparing to the power deviation caused by the constructed-aperture width variation in the subwavelength scale. In other words, a *solution to recover the influence caused by the sample thickness* has to be considered. Referring to Fig. 5-2, considering that a plane wave passes through a ideal plane rectangular aperture Σ , the diffraction optical field on the detector D behind the aperture in the far-field distance Z_0 can be evaluated by Fraunhofer diffraction, i.e.,

$$U_P(x, y) = \frac{C_0(x, y)}{\lambda Z_0} \iint_{\Sigma} U_0(\xi, \eta) \exp\left[-j \frac{2\pi}{\lambda Z_0} (x\xi + y\eta)\right] d\xi d\eta, \quad (5-4)$$

where for an aperture, $U_0(\xi, \eta) = 1$ and $C_0(x, y)$ is the phase term. What we want to do is to find a suitable orientation of the detector, which could have an analytic solution of derivation intensity. Hence, the width variation of the

constructed-aperture could be retrieved by correlating with far-field irradiance variation from the value, derivation intensity.

Referring to Fig. 5-2, considering the situation that the constructed aperture Σ' has an inclination angle ϕ to the incident plane wave, the diffraction optical field on the plane orthogonally behind the aperture Σ' in the far-field distance Z_0 can be evaluated as an oblique plane wave incident on a plane aperture Σ' , i.e.,

$$U_T(x', y) = \frac{C_0(x', y)}{\lambda Z_0} \iint_{\Sigma'} U'(\xi', \eta) \exp\left[-j \frac{2\pi}{\lambda Z_0} (x' \xi' + y \eta)\right] d\xi' d\eta, \quad (5-5)$$

where $U'(\xi', \eta) = U_0(\xi', \eta) \exp[jk\xi' \sin\phi]$, for an aperture, $U_0(\xi', \eta) = 1$, and $\exp[jk\xi' \sin\phi]$ is the relative phase of the optical field at the constructed aperture Σ' .

Substituting $U'(\xi', \eta)$ into Eq. (5-5), we have

$$U_T(x', y) = \frac{C_0(x', y)}{\lambda Z_0} \iint_{\Sigma'} U_0(\xi', \eta) \exp\left\{-j2\pi \left[\left(\frac{x'}{\lambda Z_0} - \frac{\sin\phi}{\lambda}\right)\xi' + \frac{y\eta}{\lambda Z_0}\right]\right\} d\xi' d\eta. \quad (5-6)$$

If we replace x' with $x'' + \Delta x'$, $\Delta x' = Z_0 \sin\phi$, we have

$$U_T(x'', y) = \frac{C_0(x'', y)}{\lambda Z_0} \iint_{\Sigma'} U_0(\xi', \eta) \exp\left[-j \frac{2\pi}{\lambda Z_0} (x'' \xi' + y \eta)\right] d\xi' d\eta. \quad (5-7)$$

Referring to Fig. 5-2 and comparing Eqs. (5-4) and (5-7), this means that if we position the detector at a new position, the only difference in these two equation is the diffraction aperture width of constructed aperture Σ' that effective aperture width is a/Ψ , and the tilt factor $\Psi = \cos\phi$. The analytic derivative intensity of the detector at a new position could be solved as

$$\frac{dP_z}{da} = 8 \frac{Z_0}{k\Psi} f_p(W/2, b) \text{Si}\left(\frac{kaW}{2Z_0\Psi}\right), \quad (5-8)$$

and thus can be substituted into Eq. (5-1) to retrieve the margin position of the test sample as $\bar{a} = a_0 + \Delta a$. This means that if we position the detector at a new position, which is:

- (i) Rotating the original detector D relative to the aperture in an angle ϕ to be parallel to the constructed aperture Σ' , and
- (ii) Shifting it in a distance $\Delta x' = Z_0 \sin \phi$ along the direction of $+x'$ -axis,

the corresponding derivative intensity of the detector at a new position could be deduced, and to substituted into Eq. (5-1) to retrieve the margin roughness of the test sample. While the thickness of the test sample is small compare to the aperture width, tilt factor $\Psi \cong 1$; the influence of Ψ is small and thus can be further neglected.

5.4 Simulation verifications and discussions

The feasibility of the proposed marginal roughness measurement will be numerically demonstrated as below. We first set the marginal roughness of test sample, and use a base width $a_0 = 50 \mu m$ to evaluate the base overall power $P_z(a_0)$. While moving the test sample, the corresponding overall power variation ΔP_z will be substituted into Eq. (5-1) to retrieve Δa , the deviation from marginal position to

the base width, and the exact marginal position of the test sample is simply the sum of the base width a_0 and the deviation Δa . The width of the optical ruler, b , was chosen as $6\ \mu m$, which is about 10 times the size of the light source wavelength, $632.8\ nm$ that considered here. The base-width of the aperture a_0 was $50\ \mu m$. The width of the detector W was also $50\ \mu m$, and the detector was placed behind the aperture at a distance of $30\ cm$.

Without loss of generality, two marginal roughness profiles, i.e., sine variation $a(\eta) = a_0 + \alpha \times \sin(2\pi\eta/T_d)$ and quasi-periodic variation $a(\eta) = a_0 + \frac{\alpha}{2} \times \sin(2\pi\eta/T_d) + \frac{\alpha}{2} \times \sin(2\sqrt{2}\pi\eta/T_d)$ were used to simulate the marginal roughness, and the thickness of the test sample was taken as one wavelength. The amplitude of the marginal roughness fluctuations, α , was set to $10\ nm$, and T_d was the spatial variation scale of the surface roughness.

The simulation processes are that: the marginal form of constructed-aperture is varying as the pre-setting function, $a(\eta)$. The corresponding collected power on the detector D' is evaluated numerically, and then substitute the overall power variation ΔP_z into Eq. (5-1) to get the width deviation Δa from bath width a_0 , then we get the estimated marginal roughness form: $\bar{a} = a_0 + \Delta a$ and compare it with the

pre-setting center roughness value of the constructed aperture. The retrieving results of the proposed marginal roughness measurement of different spatial scale T_d were shown in Fig. 5-3. Three different spatial variation scales, $T_d = 2b$, $5b$ and $10b$, were used to explore the feasibility and the precision limitation of the proposed measurement. The deduced results of two marginal roughness forms are shown separately in Figs. 5-3 (a) and (b) by comparing the width deviation Δa to that of the pre-setting value, and the maximum error percentage of the retrieving results were shown in the figures. The pre-setting marginal roughness was plotted in thin lines as reference, spatial variation scale $T_d = 2b$ was plotted in gray thin lines, $T_d = 5b$ was plotted in thick lines, and $T_d = 10b$ was plotted in dot lines.

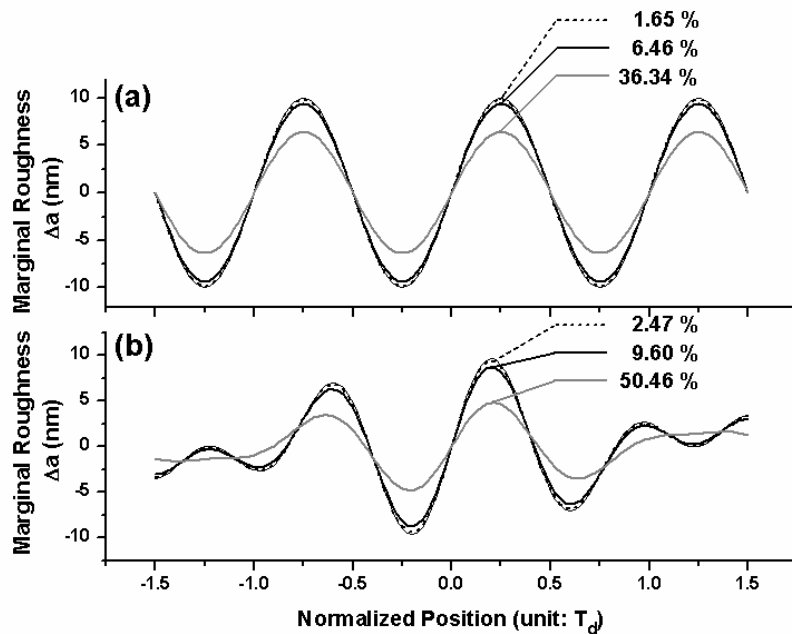
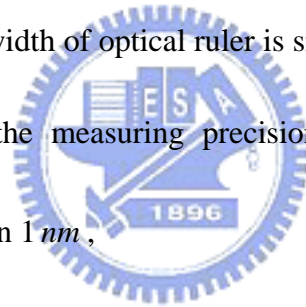


Fig. 5-3. The retrieving results of two different marginal roughness profiles: (a) sine variation. (b) quasi-periodic variation.

It can be seen that the proposed method of roughness measurement is workable. The relation between optical ruler width b and the spatial variation scale T_d determines the measurement precision of the proposed scheme. If the width of the optical ruler is $1/5$ of the spatial variation scale T_d , the precision of the proposed marginal roughness measurement will exhibit a maximum error percentage below 10%. If the width of the optical ruler is $1/10$ of the spatial variation scale T_d , the maximum error percentage will be further reduced to below 3%. From our simulation results, while the width of optical ruler is smaller than $1/5$ of the roughness spatial variation scale T_d , the measuring precision of roughness varying in an amplitude 10 nm is better than 1 nm ,



Besides, we should note that while using a shorter wavelength, the width of optical ruler could be reduced. It means that by using an optical ruler with a shorter wavelength: (1) a higher precision can always be achieved for measuring the same sample, and (2) the restriction of the spatial variation scale T_d of the test sample will be released. Furthermore, it should be noted that the proposed measurement is still workable even when the fluctuation amplitude of the marginal roughness, α , is increased to the value of one wavelength. And, the tunable embedded-aperture

interferometer configuration illustrated in the chapter 3 could be further implemented to increase the detection sensitivity.

5.5 Summary

In summary, a constructed-aperture measurement system behaving as an optical ruler was proposed to measure the marginal roughness of the test sample. The precision of the proposed method of roughness measurement is only depending on the relation between optical ruler width b and the roughness spatial variation scale T_d .

It has been numerically demonstrated that with the proposed method while the width of the optical ruler is 1/10 of the spatial variation scale T_d , the maximum error percentage of the retrieving subwavelength-scale marginal roughness could be below 3%. Better retrieving results can be further obtained by choosing an optical ruler with a shorter width.

Chapter 6

Conclusions and Future Works

6.1 Conclusions

Retrieving subwavelength information is an extensive and important topic and thus has been widely investigated. Several measurements have been proposed to retrieve the subwavelength feature detail of specimen while specimen size was in mesoscopic or nanoscopic region. While the retrieving of dynamic signature of subwavelength variation yields some more interesting information than the static features, particularly in determining physical origins and in identifying the generation mechanism, e.g., thermal characteristic, vibration, deformation. Thus, to retrieve subwavelength-scale dynamically variation is another important issue should be further investigated.

Owing to the experimental result that subwavelength feature variations of an object can affect the corresponding far-field diffraction pattern in a measurable way. The far-field optical measurement was provided as a potential approach to have real-time high-precision measure of subwavelength-scale dynamical variation of

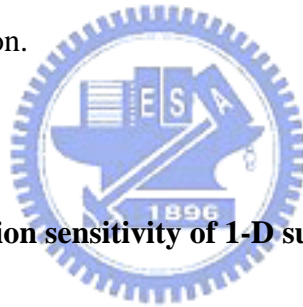
structure. Thus, in this thesis, we have investigated the approaches to retrieving dynamic signature of 1-D subwavelength-scale variation, to enhance detection sensitivity while measuring 1-D subwavelength variation, and to decouple 2-D subwavelength variation with measuring far-field optical characteristics. Besides, an extension application to identify the subwavelength-scale marginal roughness from only far-field irradiance measurement has also been proposed.

6.1.1 Retrieving of 1-D subwavelength variation information

We investigated approaches to retrieve 1-D subwavelength dynamic signatures of two simple diffraction structures, slit and rectangular aperture. Two correspondence far-field characteristics variation, irradiance and diffraction pattern was proposed as good feature quantities to retrieve 1-D subwavelength dynamic signatures.

First, with the method that retrieving subwavelength variation of the diffraction structure by measuring *far-field irradiance* variation. A physical quantity, *derivative intensity*, of these two simple diffraction situations was deduced to retrieve the 1-D dynamical subwavelength variation of these two diffraction structures. The dynamic subwavelength variation signature of both two diffraction structures are shown to be

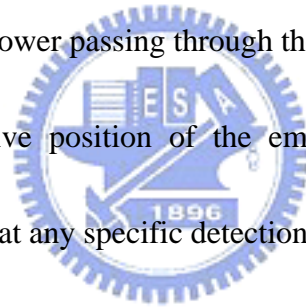
determinable from its far-field irradiance with a precision of better than 1 nm . Secondly, with the method that retrieving subwavelength variation of the diffraction structure by measuring *far-field diffraction pattern* variation. The analytical approximation relation between the dark line locations of the diffraction pattern and 1-D dynamical subwavelength variation was derived. The shifting of the diffraction pattern associated with subwavelength variation was verified holding a good linear correlation and was in an order about hundred times to the subwavelength-scale feature size variation, thus behaving as a good feature quantity to retrieve 1-D subwavelength feature variation.



6.1.2 Enhancement of detection sensitivity of 1-D subwavelength variation measurement

While measuring the structure that varying in subwavelength scale, a weak signal is usually retrieved and hence, it is a critical issue to enhance the detection sensitivity of the measurement. Therefore, effective measurement methodologies must be developed to retrieve subwavelength variation from far-field measurement with higher detection sensitivity. For avoiding damage the sample, an approach to enhance detection sensitivity without increasing the light power transmitting through the test sample was investigated.

A tunable asymmetrically-embedded-aperture interferometer configuration was proposed could efficiently enhance detection sensitivity of 1-D subwavelength variation measurement. The interferometer configuration is similar to the Mach-Zehnder interferometer structure but with an embedded aperture posited asymmetrically relative to the observing aperture with the subwavelength variation to be identified. With this configuration, the detection sensitivity of 1-D subwavelength variation measurement could be successfully increased to a desired order by increasing the light power passing through the embedded aperture. Besides, by simply shifting the relative position of the embedded aperture, the detection sensitivity could be enhanced at any specific detection width.

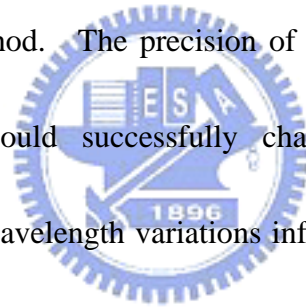


6.1.3 Deconvolution of 2-D subwavelength variation information

The investigation on far-field measurement schemes and detection sensitivity enhancement scheme of retrieving subwavelength dynamics signatures was started from that the diffraction feature was only varying only in 1-D. However, in more realistic situations, the structure may vary in two or three dimensions, and the characteristics of subwavelength variations contained in the far-field are coupled and thus will be difficult to separate. To retrieve multi-dimension subwavelength

dynamics signatures of diffraction structure, the approach to separate the coupled far-field characteristics containing multi-dimension subwavelength variation information was explored.

A three-detector, embedded-aperture interferometer configuration was proposed to record the far-field irradiance information that containing coupled 2-D subwavelength variation information of a rectangular aperture. The coupled far-field irradiance information was then separated by a blind source separation method, time-delayed correlation method. The precision of the proposed measurement was numerically demonstrated could successfully characterize the two-dimensional dynamical signatures of subwavelength variations information with error ratio below 1%.



6.1.4 One-dimension Marginal Roughness Measurement

A constructed-aperture measurement system behaving as an optical ruler was proposed to measure the marginal roughness of the test sample. The precision of the proposed method of roughness measurement is only depending on the relation between optical ruler width b and the roughness spatial variation scale T_d . It has been numerically demonstrated that with the proposed method while the width of the

optical ruler is $1/10$ of the spatial variation scale T_d , the maximum error percentage of the retrieving subwavelength-scale marginal roughness could be below 3%. From this discussion, it emphasizes that not only subwavelength-scale *temporal* variation but also subwavelength-scale *spatial* variation could be retrieved from far-field characteristics measurement.

6.2 Future works

In this thesis, we have demonstrated the feasibility of retrieving dynamic signature of 1-D subwavelength-scale variation, enhancing 1-D subwavelength variation measurement intensity, and decoupling 2-D subwavelength dynamic variation with far-field optical measurement. Besides, an extension application to identify the 1-D spatial subwavelength-scale marginal roughness from only far-field irradiance measurement has also been demonstrated to be possible.

Owing to the preliminary results we obtained as described in this thesis, we believed that the far-field measurement scheme have great potential to measure the object variation in subwavelength scale. The exploration of the development of the implementation will be one of my future works. In the following, four main directions are listed as the follow-up of my previous preliminary study. Namely,

they are:

(1). toward a more realistic diffraction structure

In the preliminary study, only simple diffraction structures, slit and rectangular aperture have been discussed. While exploring to realistic situations, diffraction structure might not be aperture, might be arbitrary shape, and might varying in more complex form. The approaches to recover the dynamical properties of such diffraction structure should be further discussed in the future.

(2). toward a more realistic, general light source properties

The far-field optical characteristics that contain subwavelength variation information might be totally different with different kinds of light source, such as coherent, incoherent, monochromatic, polychromatic light, and even white light.

In the preliminary study, only monochromatic coherent light source has been discussed, to explore the influence of light source properties on measurement will be investigated in the future.

(3). toward the achievement of higher detection sensitivity

The far-field characteristics variation caused by diffraction feature variation in subwavelength scale might be weak signal to be detected. By this concern, the approach to enhance the detection sensitivity while measuring

subwavelength-scale at every different situation will be one issue to be investigated in the future.

(4). toward the limit of common diffraction theory approach

To retrieve the subwavelength-scale variation of diffraction structure that exceeds several light wavelengths, i.e., in macroscopic region, based on scalar diffraction theory has been investigated. It is of interest to investigate the possibility to retrieve the subwavelength-scale variation while the diffraction structure is scale down, e.g., mesoscopic region. In the future, the study of the retrieval of the subwavelength variation signatures will be investigated even when the object feature size was down in wavelength or subwavelength scale.

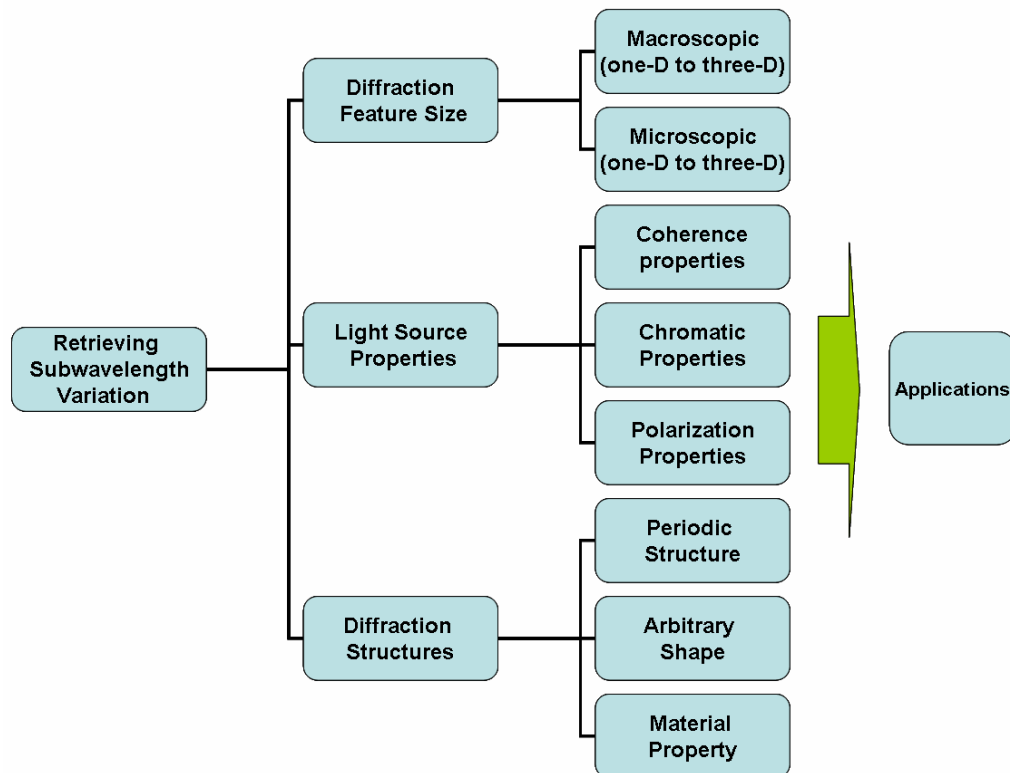


Fig. 6-1. The flow chart of my future works

Reference

- ¹ P.-T. Lee, J. R. Cao, S.-J. Choi, Z.-J. Wei, J. D. O'Brien, and P. D. Dapkus, "Operation of photonic crystal membrane lasers above room temperature," *Appl. Phys. Lett.*, **81**, 3311, (2002).
- ² J. Muys, M. Alkaisi, D. Melville, J. Nagase, P. Sykes³, G. Parguez¹ and J. Evans, "Cellular transfer and AFM imaging of cancer cells using Bioimprint," *Journal of Nanobiotechnology*, **4**:1, (2006)
- ³ L. Rockford, Y. Liu, P. Mansky, and T. P. Russell, "Polymers on Nanoperiodic, Heterogeneous Surfaces," *Phys. Rev. Lett.* **82**, 2602 (1999).
- ⁴ C. V. Nguyen, K.-J. Chao, and et al., "Carbon nanotube tip probes: stability and lateral resolution in scanning probe microscopy and application to surface science in semiconductors," *NANOTECHNOLOGY*, **12**, 363 (2001).
- ⁵ J. W. Goodman, *Introduction to Fourier Optics*, 2nd. Ed. (McGraw-Hill, New York, 1996), p. 58.
- ⁶ D. G. Fischer, "Subwavelength depth resolution in near-field microscopy," *Opt. Lett.* **25**, 1529 (2000).
- ⁷ G. E. Cragg and P. T. C. So, "Lateral resolution enhancement with standing evanescent waves," *Opt. Lett.* **25**, 46 (2000).
- ⁸ L. S. C. Pingree, M. C. Hersam, M. M. Kern, B. J. Scott, and T. J. Marks, "Spatially-resolved electroluminescence of operating organic light-emitting diodes using conductive atomic force microscopy," *Appl. Phys. Lett.*, **85**, 344, (2004).
- ⁹ T. Akiyama, M. R. Gullo, N. F. de Rooij, A. Tonin, and H.-R. Hidber, "Development of Insulated Conductive Probes with Platinum Silicide Tips for

Atomic Force Microscopy in Cell Biology,” *Jpn. J. Appl. Phys.*, 43, 2865, (2004).

¹⁰ A. A. Stekolnikov, J. Furthmüller, and F. Bechstedt, “Structural elements on reconstructed Si and Ge(110) surfaces, ” *PHYSICAL REVIEW B* **70**, 045305, (2004).

¹¹ F. Vonau, D. Aubel, G. Gewinner, C. Pirri, J. C. Peruchetti, D. Bolmont, and L. Simon, “Fermi contour imaging of the two-dimensional semimetal ErSi₂ by Fourier transform STM, ” *PHYSICAL REVIEW B* **69**, 081305, (2004).

¹² A. A. Stekolnikov, J. Furthmüller, and F. Bechstedt, “Structural elements on reconstructed Si and Ge(110) surfaces, ” *PHYSICAL REVIEW B* **70**, 045305, (2004).

¹³ F. Vonau, D. Aubel, G. Gewinner, C. Pirri, J. C. Peruchetti, D. Bolmont, and L. Simon, “Fermi contour imaging of the two-dimensional semimetal ErSi₂ by Fourier transform STM, ” *PHYSICAL REVIEW B* **69**, 081305, (2004).

¹⁴ S. Selci and M. Righini, “ Detection of subwavelength slit-width variation with irradiance measurements in the far field, ” *Opt. Lett.*, **27**, 1971 (2002).

¹⁵ J. W. Goodman, *Introduction to Fourier Optics*, 2th. Ed. (McGraw-Hill, New York, 1996), p. 38.

¹⁶ N. WALSH, T. FITZGIBBON and K.K. GHOSH, “Intraretinal axon diameter: a single cell analysis in the marmoset (*Callithrix jacchus*),” *Journal of Neurocytology*, **28**, 989 (1999).

¹⁷ B. Niggemann, T. L. Drell IV, J. Joseph, C. Weidt, K. Lang, K. S. Zaenker, and F. Entschladen, “ Tumor cell locomotion: differential dynamics of spontaneous and

-
- induced migration in a 3D collagen matrix,” *Experimental Cell Research*, **298**, 178, (2004).
- ¹⁸ Y. D. Tchoukalova, D. A. Harteneck, R. A. Karwoski, J. Tarara, and M. D. Jensen, “A quick, reliable, and automated method for fat cell sizing,” *Journal of Lipid Research*, **44**, 1795, (2003).
- ¹⁹ S.-C. Chu and J.-L. Chern, “Characterization of the subwavelength variation signature from far-field irradiance,” *Opt. Lett.*, **29**, 1045, (2004)
- ²⁰ J. W. Goodman, *Introduction to Fourier Optics*, 2th. Ed. (McGraw-Hill, New York, 1996), p. 75.
- ²¹ See <http://mathworld.wolfram.com/LeibnizIntegralRule.html>
- ²² J. W. Goodman, *Introduction to Fourier Optics*, 2th. Ed. (McGraw-Hill, New York, 1996), p. 74.
- ²³ S.-C. Chu and J.-L. Chern, “Detection of subwavelength slit-width variation with measurements in the far field by use of an embedded-aperture interferometer configuration,” *JOSA. A.*, **22**, 335, (2005)
- ²⁴ S.-C. Chu and J.-L. Chern, “Identifying the subwavelength-aperture- width variation in the far field with tunable asymmetrically- embedded- aperture interferometer configuration,” *JOSA. A.*, **22**, 1600, (2005)
- ²⁵ J. W. Goodman, *Introduction to Fourier Optics*, 2nd. Ed. (McGraw-Hill, New York, 1996), p. 74.
- ²⁶ L. Molgedey and H. G. Schuster, “Separation of a Mixture of Independent Signals Using Time Delayed Correlations,” *Phys. Rev. Lett.* **72**, 3634 (1994).
- ²⁷ S.-C. Chu and J.-L. Chern, “Retrieving two-dimensional information of the subwavelength variation from far-field irradiance,” (accepted by *JOSA. A.*) (2006)
- ²⁸ J.-Y. Ko, M.-C. Ho, J.-L. Chern, R.-R. Hsu, and C.-S. Wang, “Eigenvalue problem

approach to the blind source separation: Optimization with a reference signal,” *Phys. Rev. E*, **58**, 4872 (1998).

²⁹ J.-L. Chern, C.-C. Li, and S.-H. Tseng, “Blind phase retrieval and source separation of electromagnetic fields,” *Opt. Lett.*, **27**, 89 (2002).

³⁰ A. Cichocki and R. Unbehauen, *Neural Networks for Optimization and Signal Processing*, (Wiley, New York, 1995).



Appendix I

Review of scalar diffraction theorem

Owing to the basic formalism of this thesis is based on the scalar diffraction theorem. A short review of the most important part of the scalar diffraction theorem will be shown in this chapter.

I.1 Brief history

The evolution history of the scalar diffraction theory could be summarized in the table 1.

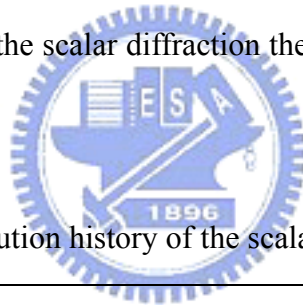


Table I.1 the evolution history of the scalar diffraction theory

Years	Figure	Important Event
1665	Grimaldi	Making the first accurate report to describe the phenomenon of the diffraction effect.
1678	Huygens	Proposing the hypothesis that the envelope of the wavefront is the superposing of the secondary wavelet of the old wavefront.
1804	Thomas Young	Proposing the concept of light interference

1818	Fresnel	Combining two concepts that “secondary wavelet” and “interference” to give the mathematical description of some diffraction patterns.
1860	Maxwell	Confirming light is an electromagnetic wave
1882	Kirchhoff	Solving the problem that light diffraction by an aperture by using two inconsistent assumptions, but giving the mathematical foundation of scalar diffraction
1894	Sommerfeld	Successfully avoiding two inconsistent assumptions in Kirchhoff’s derivations by choosing alternative Green’s functions.

I.2 Conception review the formulation of scalar diffraction theorem

In this section, the main flow of the formulation of scalar diffraction theorem will be reviewed, the detailed derivation could be found in the Ref. ^[1,2]. Consider that light propagate in a dielectric medium that is *linear, isotropic, homogeneous, and non-dispersive*, all component of the electric and magnetic field will behave identically and could be described by a single scalar wave function.

$$\nabla^2 u - \frac{n^2}{c^2} \frac{\partial^2 u}{\partial t^2} = 0, \quad (\text{I-1})$$

Where u is scalar field and n is refractive index of the medium. For a monochromatic wave, the scalar field could be written as $u(P, t) = \text{Re}\{U(P)e^{-j2\pi vt}\}$, and $U(P)$ is phasor of the wave will satisfied the Helmholtz equation

$$(\nabla^2 + k^2)U = 0 \quad (\text{I-2})$$

, where $k = 2\pi/\lambda$ is wave number.

(1) Kirchhoff and Sommerfeld theories

With the help of mathematic relation that *Green's second identity*^[3],

$$\iiint_V (U\nabla^2 G - G\nabla^2 U) dV = \iint_S \left(U \frac{\partial G}{\partial n} - G \frac{\partial U}{\partial n} \right) dS \quad (\text{I-3})$$

, Kirchhoff solved the problem that light diffraction by an aperture by choosing the

Green function G as an unit-amplitude spherical wave expending about the

observing point P_o , $G_K(P_1) = \frac{e^{jkr_{01}}}{r_{01}}$. Substituting Helmholtz equation into Eq. (I-3)

and using two inconsistent assumptions, i.e., *Kirchhoff boundary conditions*, field

U and its derivative $\frac{\partial U}{\partial n}$ vanish except in the opening Σ and across the opening

field and its derivative are equal to the value as the incident field. The field at

observing point P_o could be expressed in terms as of the disturbance U and its

normal derivative $\frac{\partial U}{\partial n}$ over the opening aperture Σ .

$$U(P_o) = \frac{1}{4\pi} \iint_{\Sigma} \left(G_K \frac{\partial U}{\partial n} - U \frac{\partial G_K}{\partial n} \right) dS \quad (\text{I-4})$$

From general potential theorem, the two Kirchhoff boundary conditions yield field is zero everywhere behind the aperture. The inconsistency of the Kirchhoff theory was removed by Sommerfeld, who chose of alternative Green's function to eliminate the necessity of imposing on both U and its derivative $\frac{\partial U}{\partial n}$ simultaneously. The Green function G he chose was two point sources that one is at observing point P_o and the other is situated at the mirror image of \tilde{P}_o on the opposite side of diffraction screen. While choosing $G_-(P_1) = \frac{e^{jk r_{01}}}{r_{01}} - \frac{e^{jk \tilde{r}_{01}}}{\tilde{r}_{01}}$, G_- vanishes on the aperture. Thus, the Kirchhoff boundary conditions may be applied U alone, yielding *first Rayleigh-Sommerfeld solution*

$$U_1(P_o) = -\frac{1}{4\pi} \iint_{\Sigma} \left(U \frac{\partial G_-}{\partial n} \right) dS = -\frac{1}{2\pi} \iint_{\Sigma} \left(U \frac{\partial G_K}{\partial n} \right) dS. \quad (I-5)$$

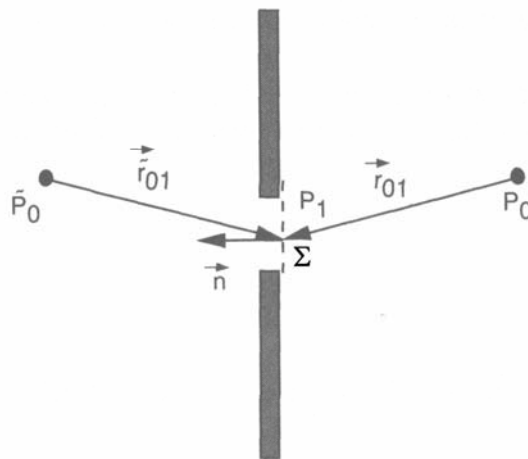


Fig. I-1. Formulation of diffraction by a screen

While choosing $G_+(P_1) = \frac{e^{jk r_{01}}}{r_{01}} + \frac{e^{jk \tilde{r}_{01}}}{\tilde{r}_{01}}$, $\frac{\partial G_+}{\partial n}$ vanishes on the aperture. Thus, the Kirchhoff boundary conditions may be applied $\frac{\partial U}{\partial n}$ alone, yielding *second*

Rayleigh-Sommerfeld solution

$$U_{II}(P_o) = \frac{1}{4\pi} \iint_{\Sigma} \left(G_+ \frac{\partial U}{\partial n} \right) dS = \frac{1}{2\pi} \iint_{\Sigma} \left(G_K \frac{\partial U}{\partial n} \right) dS. \quad (I-6)$$

From Eq. (I-3) to (I-5), it is obviously that *the Kirchhoff solution is the average of the two Rayleigh Sommerfeld solutions.*

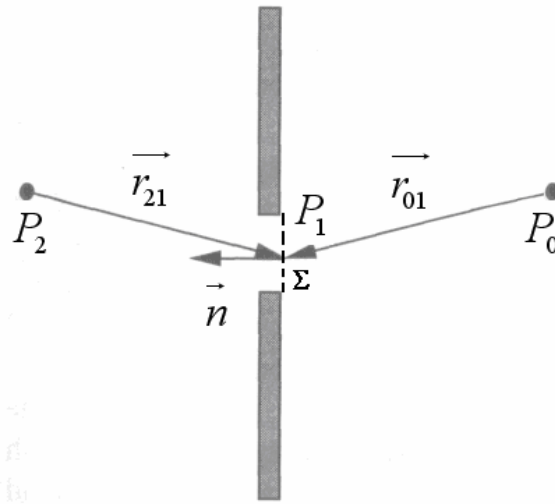


Fig. I-2. Point source illumination of a plane screen

Consider that the aperture is illuminated by a single spherical wave expending about

point P_2 , thus by substituting $U = A \frac{e^{jk r_{21}}}{r_{21}}$ into Eq. (I-3) to (I-5), all cases could be

rewrite in the form that

$$U(P_o) = \frac{A}{j\lambda} \iint_{\Sigma} \frac{e^{jk(r_{21}+r_{01})}}{r_{21}r_{01}} \Psi dS \quad (I-7)$$

$$= \frac{1}{j\lambda} \iint_{\Sigma} U(P_1) \frac{e^{jk_{r_{01}}}}{r_{01}} \Psi \, dS .$$

Kirchhoff and Sommerfeld's solutions are only different in *obliquity factor* Ψ ,

where

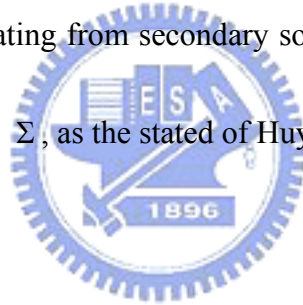
$$\Psi = \begin{cases} \frac{1}{2} [\cos(\vec{n}, \vec{r}_{01}) - \cos(\vec{n}, \vec{r}_{21})], & \text{Kirchhoff theory} \\ \cos(\vec{n}, \vec{r}_{01}), & \text{First Rayleigh - Sommerfeld solution} \\ -\cos(\vec{n}, \vec{r}_{21}) & \text{Second Rayleigh - Sommerfeld solution} \end{cases} , \quad (\text{I-8})$$

where $\cos(\vec{a}, \vec{b}) = \cos(\theta)$ and θ is the angle between vector \vec{a} and \vec{b} . Eq. (I-7)

express the observed field $U(P_0)$ is the weighted superposition of diverging

spherical waves $\frac{e^{jk_{r_{01}}}}{r_{01}}$ originating from secondary sources located at each and every

points P_1 within the aperture Σ , as the stated of Huygens-Fresnel Principle.



Several authors have compared the two formulations of the diffraction problem.

In particular, Wolf, and Marchand verified that if with the linear dimensions of the

aperture are larger comparing with the wavelength, the two theories predict essentially

the same behavior for the diffraction field in the far field, at moderate angles of

diffraction^[4].

I.3 Paraxial approximation: Fresnel and Fraunhofer diffraction

In the proceeding section, the results of Kirchhoff and Sommerfeld theories are

in more general form, in most of diffraction problem, light waves propagates along a direction which is close to the axis of optical components such as lenses or apertures.

In this case, the paraxial approximation can be used.

According to the first Rayleigh-Fresnel Sommerfeld solution, the Huygens-Fresnel principle could be stated as

$$U(P_0) = \frac{1}{j\lambda} \iint_{\Sigma} U(P_1) \frac{e^{jk r_{01}}}{r_{01}} \cos \theta dS . \quad (\text{I-9})$$

As shown in Fig. I-3, the diffraction aperture Σ is assumed to lie in (ξ, η) plane and is illuminated in the positive direction. While calculating different wavefield across the (x, y) plane at different normal distance from diffraction aperture, Fresnel and Fraunhofer approximation allow diffraction pattern calculation to be reduced to comparatively simple mathematical manipulations, i.e., Fresnel and Fraunhofer diffraction formula.

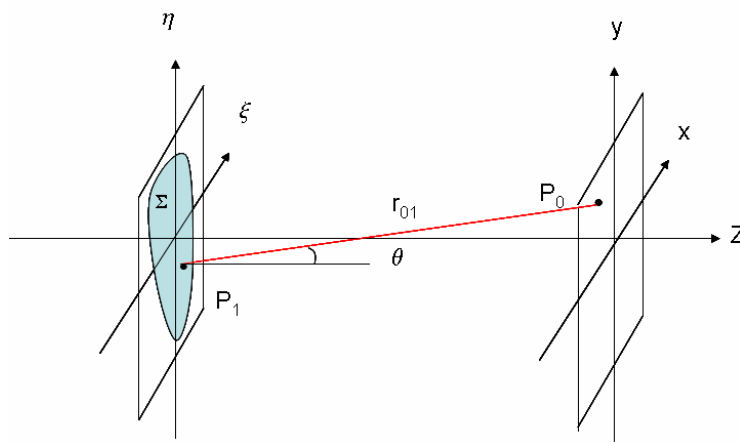


Fig. I-3. Diffraction Geometry

(1) Fresnel diffraction formula

For the situation that the observing point is not far away from the optical axis, i.e., satisfying the Fresnel approximation, $z^3 \gg \frac{\pi}{4\lambda} [(x-\xi)^2 + (y-\eta)^2]_{\max}^2$, by using the binomial approximation in exponent, the resulting expression for the field at (x, y) plane could be calculated by Fresnel diffraction formula:

$$\begin{aligned} U_o(x, y) &= \frac{e^{jkz}}{j\lambda z} \iint U(\xi, \eta) e^{j\frac{\pi}{\lambda z} [(x-\xi)^2 + (y-\eta)^2]} d\xi d\eta \quad (\text{I-9}) \\ &= \frac{e^{jkz}}{j\lambda z} e^{j\frac{\pi}{\lambda z} (x^2 + y^2)} \iint \left[U(\xi, \eta) e^{j\frac{\pi}{\lambda z} (\xi^2 + \eta^2)} \right] e^{-j\frac{2\pi}{\lambda z} (x\xi + y\eta)} d\xi d\eta. \end{aligned}$$

(2) Fraunhofer diffraction formula

If in addition to Fresnel approximation the stronger Fraunhofer approximation $z \gg \frac{\pi}{\lambda} (\xi^2 + \eta^2)_{\max} = \frac{\pi}{\lambda} D^2$ is satisfied, the quadratic phase factor $e^{j\frac{\pi}{\lambda z} (\xi^2 + \eta^2)}$ in Eq. (I-9) is approximated unity over the entire aperture. Thus the expression for the field at (x, y) plane could be calculated by Fraunhofer diffraction formula:

$$U_o(x, y) = \frac{e^{jkz}}{j\lambda z} e^{j\frac{\pi}{\lambda z} (x^2 + y^2)} \iint U(\xi, \eta) e^{-j\frac{2\pi}{\lambda z} (x\xi + y\eta)} d\xi d\eta. \quad (\text{I-10})$$

It should be further noted that for the Fresnel approximation to yield accurate result, it is not necessary that the higher-order terms of the expansion be small, only that they not change the value of Fresnel diffraction integral significantly. The discussion on

the validity of Fresnel diffraction integral could be founded in Ref. [5].

I.4 Angular spectrum method

Another useful approach to calculate the scalar diffraction is angular spectrum approach [6], which has been widely applied to electrodynamics, optics, and acoustics.

We give a brief review of its theory. Consider the complex-amplitude distribution

$U(x, y, Z=0)$ in the XY-plane at $Z=0$, by simply applying the Fourier transform on $U(x,$

$y, z=0$), it could be treated as the superposition of several plane wave each containing

different spatial frequency (f_x, f_y) . The weighting of the superposition is named as

angular spectrum

$$A(f_x, f_y; Z = 0) = \int_{-\infty}^{\infty} \int_{-\infty}^{\infty} U(x, y, Z = 0) \exp[-i2\pi(xf_x + yf_y)] dx dy ,$$

(I-11)

where $a(x, y, z=0)$ is the inverse Fourier transform of it's angular spectrum

$$U(x, y, Z = 0) = \int_{-\infty}^{\infty} \int_{-\infty}^{\infty} A(f_x, f_y; Z = 0) \exp[i2\pi(xf_x + yf_y)] df_x df_y \quad (I-12)$$

Consider the complex-amplitude distribution $a(x, y, Z=z)$ in the XY-plane at $z=Z$, the

angular spectrum of field $a(x, y, Z=z)$ will be

$$A(f_x, f_y; Z = z) = \int_{-\infty}^{\infty} \int_{-\infty}^{\infty} a(x, y, Z = z) \exp[-i2\pi(xf_x + yf_y)] dx dy . \quad (I-13)$$

Again, field $a(x, y, Z=z)$ is the inverse Fourier transform of it's angular spectrum

$$U(x, y, Z = z) = \int_{-\infty}^{\infty} \int_{-\infty}^{\infty} A(f_x, f_y; Z = z) \exp[i2\pi(xf_x + yf_y)] df_x df_y. \quad (\text{I-14})$$

At source free points and consider that light propagate in a dielectric medium that is linear, isotropic, homogeneous, and non-dispersive, $a(x, y, Z=z)$ satisfied Helmholtz eq, $(\nabla^2 + k^2)U = 0$, thus we have

$$\frac{d^2}{dz^2} A(f_x, f_y; Z = z) + (2\pi)^2 \exp(1 - f_x^2 - f_y^2) A(f_x, f_y; Z = 0). \quad (\text{I-15})$$

The propagation of the angular spectrum could be derived as an elementary solution of this equation and was written as

$$A(f_x, f_y; Z = z) = A(f_x, f_y; Z = 0) \exp\left(j2\pi\sqrt{1 - f_x^2 - f_y^2} z\right) \quad (\text{I-16})$$

The physical interpretation of the angular spectrum method is that the every simple plane-wave component containing different spatial frequency are solutions of Maxwell's equations in a homogeneous environment can be expressed as

$$a(x, y, z) = A_0 \exp[i(2\pi / \lambda)(x\sigma_x + y\sigma_y + z\sigma_z)]. \quad (\text{I-17})$$

Where λ is the wavelength of the light and $\sigma = \left(\sigma_x = \lambda f_x, \sigma_y = \lambda f_y, \sigma_z = \sqrt{1 - \sigma_x^2 - \sigma_y^2}\right)$ is a unit vector specifying the direction of propagation and, A_0 is a complex vector representing the magnitude and one state of polarization of the E -field at the origin of the coordinate system. On the one hand, σ_z will be real-valued if $\sigma_x^2 + \sigma_y^2 \leq 1$, in which case the plane wave is said to be homogeneous or propagating wave. If $\sigma_x^2 + \sigma_y^2 > 1$, then σ_z becomes imaginary and the plane wave is called inhomogeneous or evanescent wave.

Because the evanescent waves carry no energy from the diffraction aperture, so we can rewrite the disturbance observed at (x, y, z) in terms of the initial angular spectrum as

$$a(x, y, Z = z) = \int_{-\infty}^{\infty} \int_{-\infty}^{\infty} A(\sigma_x, \sigma_y; Z = 0) \exp\left(j \frac{2\pi}{\lambda} \sqrt{1 - \sigma_x^2 - \sigma_y^2}\right) \times \text{circ}\left(\sqrt{\sigma_x^2 + \sigma_y^2}\right) \left[i \frac{2\pi}{\lambda} (x\sigma_x + y\sigma_y)\right] d\frac{\sigma_x}{\lambda} d\frac{\sigma_y}{\lambda} \quad (\text{I-18})$$

It should be noted that the angular spectrum approach and the first Rayleigh-Sommerfeld solution yield identical prediction of diffraction field ^[7].

¹ M. Gu, *Advanced Optical Imaging Theory*, Ed. (Springer, Berlin, 1999).

² J. W. Goodman, *Introduction to Fourier Optics*, 2th. Ed. (McGraw-Hill, New York, 1996).

³ See <http://mathworld.wolfram.com/GreensIdentities.html>

⁴ E. Wolf and E. W. Marchand, "Comparison of the Kirchhoff and Rayleigh-Sommerfeld theories of diffraction at an aperture," *JOSA.*, 54:587, (1964)

⁵ W. H. Southwell, "Validity of the Fresnel approximation in the near field," *JOSA.*, 71:7, (1981)

⁶ J. W. Goodman, *Introduction to Fourier Optics*, 2th. Ed. (McGraw-Hill, New York, pp. 55-61, (1996).

⁷ G. C. Sherman, "Application of the convolution theorem to Rayleigh's integral formulas," *JOSA.*, 57:546, (1967)

Appendix II

Blind source separation problem

In the chapter titled as “Deconvolution of 2-D subwavelength variation information,” we adopted “Time-delayed correlation method” to solve the “Blind signal separation problem.” In this section, we give the definition of “Blind signal separation problem” and literature review the some approaches to solve the “Blind signal separation problem” and detailed the approach of “Time-delayed correlation method.”



II.1 Introduction to blind source separation problem

“The blind source separation problem could be defined as the problem of separating and estimating of multiple independent source signals from an array of sensors without knowing the characteristic of the transmission channels” ^[1]. Blind source separation has been an intriguing issue for a long time, partially due to its similarity to the human experience, e.g., the cocktail party effect ^[2]. The problem of source separation appears in many contexts. The simplest situation occurs for two speakers. If the mixture of their voices reaches two microphones, one wants to separate both

sources such that each detector registers only one voice ^[3]. Further examples, involving many sources and receivers, are the separation of odors in a mixture by an array of sensors and the parsing of the environment into different objects by our visual system ^[4]. Because of the complexity inherent in these problems, blind source separation has stood as an unsolved problem in history.

The classical blind signal separation problem could be illustrated in the Fig. II-1. The blind signal separation methods could recover the mixing independent source signals by the detected signal.

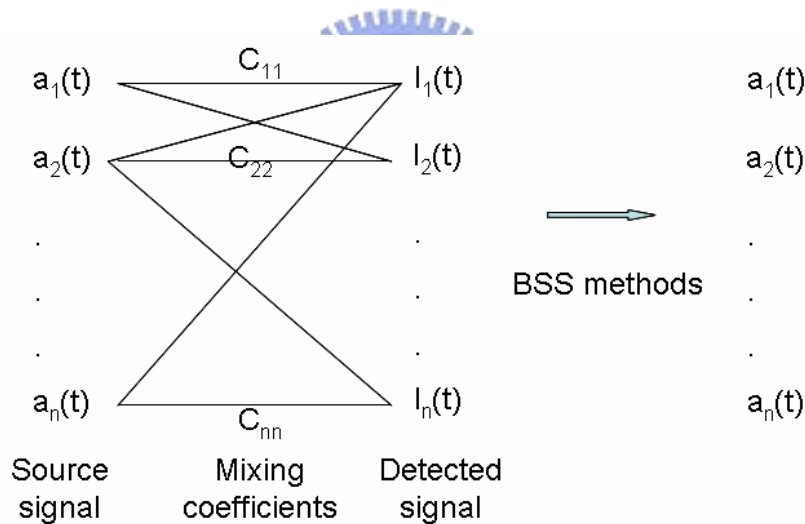


Fig. II-1. Schematic diagrams of the blind source separation problems

Let us assume that we have n detectors each of which is sensitive to a set of unknown statistically independent signals $a_i(t), (i = 1, 2, \dots, n)$, i.e., $\langle a_i(t)a_j(t') \rangle = K_i(t-t')\delta_{ij}$. Suppose the output signal $I_i(t), (i = 1, 2, \dots, n)$ of the detectors are linear combinations of the input signals $a_i(t)$, i.e., the system is described by the set of

equations

$$I_i(t) = \sum_{j=1}^n C_{ij} a_j(t); (i = 1, 2, \dots, n) \quad (\text{II-1})$$

, where C_{ij} are the mixing coefficients. It could be written in compact matrix form

$I = CA$. The term “Blind Signal” refers to the mixing signal without knowing its

mixing model. The blind source separation problem is to discriminate the input

signals under the assumption that the input signals are mutually statistically

independent. On the other hand, there are only n detected signals available. The

classical problem is how one determines the coefficients C_{ij} and the source strengths

$K_i(0)$ from a measurement of $I_i(t)$. Because the matrix C is generally not

symmetric and the source strengths are not available, the total unknown number of

variables is $n(n+1)$. Such a problem was first addressed and solved by J. Herault and

C. Jutten. They proposed an adaptive neural network to perform this task ^[5]. It

decorrelates the incoming signals via an inhibitory interaction between the output

neurons which has been further developed by many researchers ^[6,7,8,9,10,11].

II.2 Time-delayed correlation method

Unlike most methods using neural network approach to solve the blind source

separation problem, Molgedey and Schuster (MS) proposed using time-delayed

correlation and eigenvalue problem approach to separate a mixture of independent

signals ^[12]. The method was abbreviated as M-S method, which will be detailed as followed.

The correlations of two signals $a_i(t)$ and $a_j(t)$ could be represented as $\langle a_i(t)a_j(t) \rangle$. The time-delayed correlation is the correlation of one signals $a_i(t)$ and time-delay signal $a_j(t+\tau)$, i.e., $\langle a_i(t)a_j(t+\tau) \rangle$. The concept of time-delayed correlation is coming form the concept of “independent source signals.” For n statistically independent signals $a_i(t), (i=1,2,\dots,n)$, two different signals are independent, thus will satisfy the condition

$$\langle a_i(t)a_j(t) \rangle = 0. \text{ (for all } i \neq j \text{)} \quad \text{(II-2)}$$

The time-delayed correlation of two independent signals will satisfy the condition

$$\langle a_i(t)a_j(t+\tau) \rangle = 0. \text{ (for all } i \neq j \text{)} \quad \text{(II-3)}$$

For single source signal $a_i(t)$ will satisfy the condition

$$\langle a_i(t)^2 \rangle > 0. \text{ (for all } i \text{)}. \quad \text{(II-4)}$$

The self time-delayed correlation satisfy the condition

$$\langle a_i(t)a_i(t+\tau) \rangle > 0. \text{ (for all } i \text{)}. \quad \text{(II-5)}$$

The above four relations are the basic concept of time-delayed correlation method.

M-S method introduces the additional assumption that the mean value of the source signal is zero, i.e.,

$$\langle a_i(t) \rangle = 0. \text{ (for all } i \text{)}. \quad \text{(II-6)}$$

From equation (II-3) and (II-5), the time-delayed correlation of the source signals could be represented as

$$\langle a_i(t)a_j(t+\tau) \rangle = K(\tau)\delta_{ij}. \quad (\text{II-7})$$

Constructing two matrices, the *symmetrical correlation matrix* $M_{ij} = \langle I_i(t)I_j(t) \rangle$ and the *time delayed correlation matrix* $\bar{M}_{ij} = \langle I_i(t)I_j(t+\tau) \rangle$. The matrix form could be represented as

$$\begin{aligned} M &= \langle I(t)I^T(t) \rangle \\ \bar{M} &= \langle I(t)I^T(t+\tau) \rangle \end{aligned} \quad (\text{II-8})$$

For source signals satisfying the above the five assumptions, (II-2) to (II-6), the blind source separation problem becomes an eigenvalue problem where $(M\bar{M}^{-1})C = \lambda C$. While we solving the mixing coefficients C_{ij} , it could be easily adopted to solve the source signal $a_i(t)$. The detail derivation will be addressed bellow.

The matrix representation of relations of source signals and detected signals is

$I(t) = CA(t)$, thus $I(t)^T = (CA(t))^T = A(t)^T C^T$. Substituting it into Eq. (II-8), we have

$$\begin{aligned} M &= \langle CA(t)A(t)^T C^T \rangle = C \langle A(t)A(t)^T \rangle C^T = C \Lambda C^T \\ \bar{M} &= \langle CA(t+\tau)A(t+\tau)^T C^T \rangle = C \langle A(t+\tau)A(t+\tau)^T \rangle C^T = C \bar{\Lambda} C^T \end{aligned} \quad (\text{II-9})$$

Where

$$\begin{aligned}\Lambda &= \langle A(t)A(t)^T \rangle \\ \bar{\Lambda} &= \langle A(t+\tau)A(t+\tau)^T \rangle\end{aligned}\quad . \quad (\text{II-10})$$

The element of the Λ , $\bar{\Lambda}$ are $\Lambda_{ij} = K_i(0)\delta_{ij}$, $\bar{\Lambda}_{ij} = K_i(\tau)\delta_{ij}$. Dividing the *symmetrical correlation matrix* by *time delayed correlation matrix*, we have

$$\begin{aligned}M\bar{M}^{-1} &= C\Lambda C^T (C\bar{\Lambda}C^T)^{-1} \\ &= C\Lambda C^T (C^T)^{-1} \bar{\Lambda}^{-1} C^{-1} \quad . \\ &= C\Lambda\bar{\Lambda}^{-1}C^{-1}\end{aligned}\quad (\text{II-11})$$

By multiplying mixing coefficient matrix C , we have $(M\bar{M}^{-1})C = C(\Lambda\bar{\Lambda}^{-1})$. From

Eq (II-10), we know that $(\bar{\Lambda}^{-1})_{ij} = \left(\frac{1}{K_i(\tau)}\right)\delta_{ij}$, thus

$$\Lambda\bar{\Lambda}^{-1} = \begin{pmatrix} K_i(0) \\ K_i(\tau) \end{pmatrix} \delta_{ij} D = \lambda D, \quad (\text{II-12})$$

where D is identity matrix. By substituting Eq. (II-12) into Eq. (II-11), we have

$(M\bar{M}^{-1})C = \lambda C$, which is an eigenvalue problem. By solving the eigenvalue

problem, we can have the mixing coefficients matrix C and so do source signal

matrix $A = C^{-1}I$. In a word, by using M-S method, we can simply solve the blind

source separation problem by solving eigenvalue problem.

¹ A. Cichocki and R. Unbhauen, "Neural (London) Networks for Optimization and Signal Processing," JOHN WILEY & SONS, 1993, pp.461-474

² J. Maddox, "Cocktail party effect made tolerable," Nature, **369**, 517 (1994).

³ H. W. Strube, "Separation of several speakers recorded by two microphones (cocktail-party processing)," Signal Processing 3, 355, (1981).

⁴ C. M. Gray, A. K. Engel, W. Singer, and P. Konig, "Oscillatory responses in cat

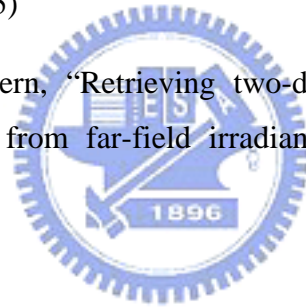
visual cortex exhibit inter-columnar synchronization which reflects global stimulus properties," *Nature (London)*, 338, 334 (1989).

- ⁵ J. Herault and C. Jutten, "Space or time adaptive signal processing by neural network models," in *AIP Conf. Proc.*, snowbird, UT 1986, pp.206-211.
- ⁶ C. Jutten and J. Herault, "Independent component analysis (INCA) versus principal component analysis", in *Signal Processing IV*, Ed. J.Llacoume, Elsevier, Amsterdam, 1988, pp.643-646.
- ⁷ C. Jutten and J. Herault, "Blind separation of sources, Part I: An adaptive algorithm based on neuromimetic architecture", *Signal Processing*, vol.24, 1991, pp.1-10.
- ⁸ J. Cardoso, "Source separation using higher order moments," *Proc. IEEE ICASSP*, 1989, vol.4, pp.2109-2112.
- ⁹ J. Cardoso, "Super-symmetric decomposition of the fourth-order cumulant tensor; Blind identification of more sources than sensors," *Proc. IEEE ICASSP-91* Toronto, 1991, pp.3109-3112.
- ¹⁰ J. Vandewalle and B. De Moore, "A variety of applications of singular value decomposition in identification and signal processing," in *SVD and Signal Processing*, ed. E. F. Deprettere, *Elsevier, Amsterdam*, 1988, pp.43-91.
- ¹¹ A. Cichocki and T. Lobos, "Adaptive analogue network for real-time estimation of basic waveforms of voltages and currents," *IEE Proc. Part-C*, vol.139, 1992, pp. 343-350.
- ¹² L. Molgedey and H. G. Schuster, "Separation of a Mixture of Independent Signals Using Time Delayed Correlations", *Physical Review Letters*, vol.72, no.23, pp. 3634-3637 JUNE 1994.

Publication List

Journal Papers

1. S.-C. Chu and J.-L. Chern, "Characterization of the subwavelength variation signature from far-field irradiance," *Opt. Lett.*, 29, 1045, (2004)
2. S.-C. Chu and J.-L. Chern, "Detection of subwavelength slit-width variation with measurements in the far field by use of an embedded-aperture interferometer configuration," *JOSA. A.*, 22, 335, (2005)
3. S.-C. Chu and J.-L. Chern, "Identifying the subwavelength-aperture- width variation in the far field with tunable asymmetrically- embedded- aperture interferometer configuration," *JOSA. A.*, 22, 1600, (2005)
4. S.-C. Chu and J.-L. Chern, "No-Loss bent lightpipe with an equiangular spiral," *Opt. Lett.*, 30, 3006, (2005)
5. S.-C. Chu and J.-L. Chern, "Retrieving two-dimensional information of the subwavelength variation from far-field irradiance," (Accepted by *JOSA. A.*) (2006)



Conference Papers

※ Optics and Photonics Taiwan

1. S.-C. Chu and Mao-Hong Lu, "The design of a dense wavelength division de-multiplexer by using grating-prism configuration." (Oral, 2003)
2. S.-C. Chu and J.-L. Chern, "No-loss bent lightpipe." (Oral, 2005)

※ Annual meeting of Chinese Physical Society

1. S.-C. Chu and J.-L. Chern, "Retrieving the two-dimension information of subwavelength variation from far-field irradiance." (Oral, 2006)
2. S.-C. Chu and J.-L. Chern, "Exploration of subwavelength dynamic variation with far-field irradiance." (Poster, 2006)

※ International Optical Design Conference

1. S.-C. Chu and J.-L. Chern, "Equiangular-spiral non-loss bent lightpipe and its applications." (Oral, 2006)